Cell Reports

Article

Visual-area-specific tonic modulation of GABA release by endocannabinoids sets the activity and coordination of neocortical principal neurons

Graphical abstract

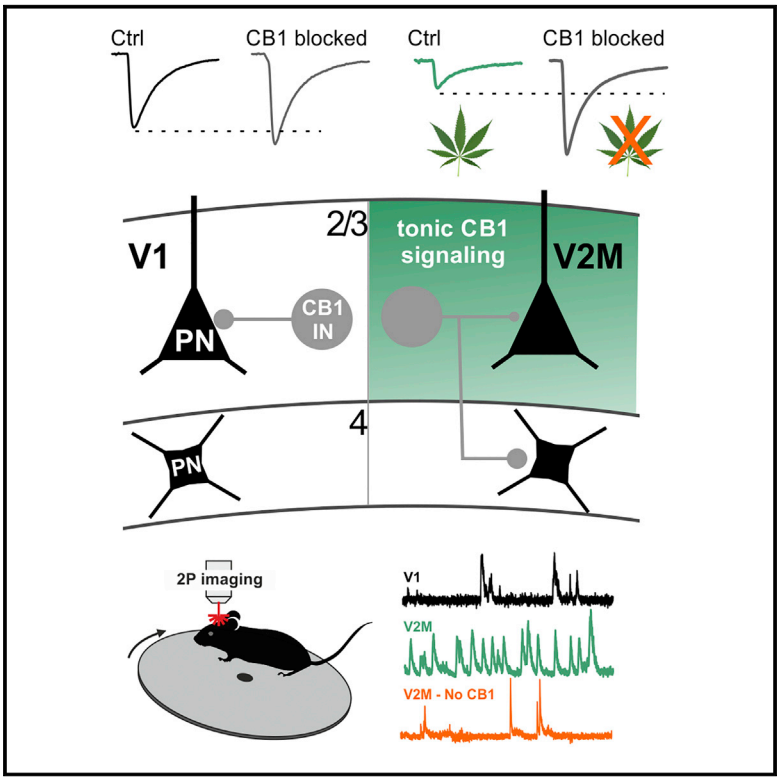

Highlights

- CB1$^+$ basket cells exhibit visual-area-specific morphology and connectivity patterns
- Tonic CB1 signaling underlies high pyramidal neurons (PN) activity in V2M but not V1
- Tonic CB1 signaling differentially modulates PN-correlated activity in V1 and V2M
- Numerical simulations capture specific CB1-dependent firing dynamics of V1 and V2M

Authors

Fani Koukouli, Martin Montmerle, Andrea Aguirre, ..., Nelson Rebola, Alberto Bacci, Joana Lourenço

Correspondence

alberto.bacci@icm-institute.org (A.B.), joana.lourenco@icm-institute.org (J.L.)

In brief

Cannabinoid receptor type 1 (CB1) basket cells are prominent but elusive cortical interneurons, inhibiting the soma of principal neurons. Koukouli et al. show that CB1$^+$ interneurons exhibit specific connectivity properties in distinct visual cortical areas and differently control the activity and coordination of primary (V1) and associative (V2M) visual areas.

Koukouli et al., 2022, Cell Reports *40*, 111202
August 23, 2022
https://doi.org/10.1016/j.celrep.2022.111202

CellPress

Cell Reports

CellPress
OPEN ACCESS

Article

Visual-area-specific tonic modulation of GABA release by endocannabinoids sets the activity and coordination of neocortical principal neurons

Fani Koukouli,[1,6] Martin Montmerle,[1,6] Andrea Aguirre,[1] Marcel De Brito Van Velze,[1] Jérémy Peixoto,[1] Vikash Choudhary,[1] Marjorie Varilh,[2] Francisca Julio-Kalajzic,[2] Camille Allene,[1] Pablo Mendéz,[3] Yann Zerlaut,[1] Giovanni Marsicano,[2] Oliver M. Schlüter,[4,5] Nelson Rebola,[1] Alberto Bacci,[1,7,*] and Joana Lourenço[1,8,*]

[1]ICM – Institut du Cerveau, Sorbonne Université, INSERM, CNRS, Paris, France
[2]INSERM, U1215 NeuroCentre Magendie, University of Bordeaux, 33077 Bordeaux, France
[3]Instituto Cajal (CSIC), Madrid, Spain
[4]Department of Psychiatry and Psychotherapy, University Medical Center Göttingen, Göttingen, Germany
[5]Department of Neuroscience, University of Pittsburgh, Pittsburgh, PA, USA
[6]These authors contributed equally
[7]Senior author
[8]Lead contact
*Correspondence: alberto.bacci@icm-institute.org (A.B.), joana.lourenco@icm-institute.org (J.L.)
https://doi.org/10.1016/j.celrep.2022.111202

SUMMARY

Perisomatic inhibition of pyramidal neurons (PNs) coordinates cortical network activity during sensory processing, and this role is mainly attributed to parvalbumin-expressing basket cells (BCs). However, cannabinoid receptor type 1 (CB1)-expressing interneurons are also BCs, but the connectivity and function of these elusive but prominent neocortical inhibitory neurons are unclear. We find that their connectivity pattern is visual area specific. Persistently active CB1 signaling suppresses GABA release from CB1 BCs in the medial secondary visual cortex (V2M), but not in the primary visual cortex (V1). Accordingly, *in vivo*, tonic CB1 signaling is responsible for higher but less coordinated PN activity in the V2M than in the V1. These differential firing dynamics in the V1 and V2M can be captured by a computational network model that incorporates visual-area-specific properties. Our results indicate a differential CB1-mediated mechanism controlling PN activity, suggesting an alternative connectivity scheme of a specific GABAergic circuit in different cortical areas.

INTRODUCTION

Integration of sensory information into perception is accomplished by cortical circuits formed by a multitude of cellular subtypes that connect with each other following a detailed blueprint (Pfeffer et al., 2013; Kepecs and Fishell, 2014; Allene et al., 2015; Tremblay et al., 2016). Sensory systems are highly organized and hierarchal. Sensory information is relayed (via the thalamus) to the primary sensory neocortical areas, mainly in layer 4 (L4), and it is then passed along to other cortical layers in a stereotyped sequence before being sent to higher-order associative cortical areas. In parallel, higher-order cortical areas send information to primary cortices, modulating their activity (Larkum, 2013; Keller et al., 2020). These loops allow information to travel across different sensory areas via direct connections and cortico-thalamic pathways (Larkum, 2013; Harris and Shepherd, 2015; Glickfeld and Olsen, 2017). Higher-order sensory cortices are integrative areas receiving bottom-up (or sensory) as well as top-down (or contextual) information, playing a major role in decoding specific sensory features and in predictive processing and behavior (Glickfeld and Olsen, 2017; Clancy et al., 2019; Keller et al., 2020; Murgas et al., 2020; Jin and Glickfeld, 2020).

Fast synaptic GABAergic inhibition is crucial for shaping spontaneous and sensory-evoked cortical activity (Isaacson and Scanziani, 2011; Tremblay et al., 2016; Lourenço et al., 2020b). Inhibitory GABAergic neurons (interneurons or INs) are highly heterogeneous, and this rich diversity results in efficient orchestration of cortical activity via a highly specialized division of labor of different interneuron types (Ascoli et al., 2008; Tremblay et al., 2016; Lourenço et al., 2020b; Isaacson and Scanziani, 2011; Freund and Katona, 2007). In particular, perisomatic-region-targeting basket cells (BCs) form inhibitory synapses mainly near the cell soma of pyramidal neurons (PNs) and, thus, control spike generation and timing (Buzsaki and Wang, 2012). A prominent perisomatic-region-targeting interneuron type, the parvalbumin (PV)-expressing BC, is important during sensory information processing and drives cognition-relevant fast network oscillations (Atallah et al., 2012; Lee et al., 2012; Wilson et al., 2012; Freund and Katona, 2007; Buzsaki and Wang, 2012; Deleuze et al., 2019). However, PV BCs are not the only inhibitory cell type controlling the perisomatic region of neocortical PNs (Freund and Katona, 2007; Armstrong and Soltesz, 2012). Most notably, interneurons expressing high levels of cannabinoid receptor type

1 (CB1) also form inhibitory synapses with PN cell bodies (Bodor et al., 2005). These cells have been traditionally identified as expressing cholecystokinin (CCK), especially in the hippocampus (Marsicano and Lutz, 1999; Katona et al., 1999; Hefft and Jonas, 2005; Daw et al., 2009; Dudok et al., 2021), and they form GABAergic synapses that are much less reliable (Wilson et al., 2001; Hefft and Jonas, 2005; Daw et al., 2009). However, the properties and roles of CB1 BCs within neocortical circuits remain elusive. In particular, whether CB1 BCs efficiently control neocortical PN firing is unknown.

Endogenous cannabinoids (endocannabinoids, eCBs) acting on CB1 potently inhibit release of GABA, resulting in several forms of inhibitory plasticity, such as depolarization-induced suppression of inhibition (DSI) and long-term depression of inhibitory synapses (LTDi) (Hajos et al., 2000; Maejima et al., 2001; Wilson and Nicoll, 2001; Kano et al., 2009; Castillo et al., 2012; Marsicano et al., 2002; Younts and Castillo, 2014). Both forms of plasticity rely on retrograde signaling of eCBs, which are synthesized on demand in the postsynaptic PNs by intracellular Ca^{2+} increase or metabotropic glutamate receptor (mGluR) activation and delivered to presynaptic terminals of CB1-expressing GABAergic interneurons (Kano et al., 2009; Castillo et al., 2012). In addition to this on-demand eCB modulation of neurotransmitter release, in the hippocampus, CB1 receptors have been reported to be persistently active, leading to constant signaling and tonic inhibition of GABA release from CB1 interneurons (Losonczy et al., 2004; Neu et al., 2007; Lee et al., 2010).

Using a mouse line specifically tagging CB1-expressing neurons (CB1-tdTomato mice) (Winters et al., 2012), here we set out to study the morpho-functional features of neocortical CB1 BCs and test whether these cells efficiently control PN activity in the visual cortex.

We found that CB1 expression is generally stronger in associative than in primary sensory cortical areas. We then focused on the primary visual cortex (V1) and its associative, higher-order medial secondary area (medial secondary visual cortex [V2M]), which exhibits strong CB1 expression. We describe a differential morphological and functional connectivity scheme of CB1 interneurons in the V1 and V2M. Tonic CB1 modulation conferred specific weak presynaptic properties at inhibitory synapses from CB1 BCs only in L2/3 of the V2M. This area-specific connectivity and eCB modulation of GABA release from CB1 BCs was responsible for lower PN activity in the V1 compared with the V2M *in vivo*. Visual-area-specific tonic CB1 signaling differently set the amount of correlated activity of PNs in the two visual areas. We provide experimental and numerical evidence that cortical-area-specific connectivity of CB1 BCs and CB1 signaling at their synapses are responsible for differently setting firing dynamics and coordination of PNs in the V1 and V2M.

RESULTS

Differential CB1 expression and morphological properties of CB1-positive interneurons in the V1 and higher-order visual cortex

CB1 modulates neurotransmitter release (Castillo et al., 2012), but the exact pattern of CB1 expression across layers in the V1 and V2M has not yet been examined (but see Yoneda et al., 2013). We therefore performed CB1 immunofluorescence analysis in wild-type mice (Figure 1A). Overall, CB1 expression was highest in L1 of the V1 and L2/3 of the V2M (Figures 1A–1C). To compare the laminar expression between the two areas, we binned these data into distances corresponding to cortical layers (Figure 1C). In the V1, the average intensity of peak-normalized fluorescence gradually decreased from L1 to L4 (L1 = 70.5% ± 2.2%, L4 = 38.7% ± 2.3%, n = 11 animals) to then increase and reach another peak in L6 (66.3% ± 3.2%; Figures 1B, black line, and 1C, black bars). In contrast, in the V2M, the peak-normalized fluorescence from the pia to white matter was always between a maximum in L2/3 and a minimum in L5 (L2/3 = 70.7% ± 3.3%, L5 = 57.3% ± 3.3%; Figures 1B, red line, and 1C, red bars). We found that, except in L6 and L1, the level of expression of CB1 was higher in all other cortical layers of the V2M than V1. In particular, in layers L2/3, 4, and 5 of the V1, CB1 expression was weaker than in the V2M (52.6 ± 2.2, 38.77 ± 2.3, 41% ± 2.2%, respectively; $p = 0.0001$, $p < 0.0001$, $p = 0.0006$, respectively; Friedman, repeated-measures, post hoc analysis with correction for multiple comparisons, Sidak's multiple comparisons test; Figures 1B and 1C). The asymmetrical distribution of CB1 immunostaining between the V1 and associative, higher-order visual areas (including the V2M) did not depend on the slice angle because it was also preserved in sagittal brain slices (Figures S1A and S1B).

CB1 is not expressed exclusively by GABAergic interneurons (Marsicano and Lutz, 1999; Katona et al., 2006; Marinelli et al., 2009). Therefore, we crossed CB1-tdTomato with GAD67-GFP mice to quantify CB1-expressing GABAergic cells in the two visual areas (Figure S1C). We found that the large majority of CB1 cells co-expressed GAD67 (Figure S1D), and their density was higher in L2/3 of the V2M compared with the V1 (Friedman, repeated-measures, post hoc analysis with correction for multiple comparisons, Sidak's multiple comparisons test, $p = 0.0277$; Figure S1E). CB1 cells did not co-localize with molecular markers of cortical interneuron subclasses originating from the medial ganglionic eminence (Figure S2A), but the majority (~60%) of CB1 cells co-localized with 5-hydroxytryptamine 3A receptor ($5HT_{3A}R$) (Figures S2C and S2D; Tremblay et al., 2016; Paul et al., 2017). *In situ* hybridization using CB_1 (*Cnr1*) and *CCK (Cck)* mRNA probes revealed co-localization of tdTomato-expressing neurons with *CB1* (>75%) and *CCK* (>40%; Figure S2G).

To test whether higher CB1 immunoreactivity in deeper cortical layers of the V2M was due to differential connectivity, we performed whole-cell, patch-clamp recordings from L2/3 multipolar CB1 BCs, visually identified as expressing bright fluorescence in CB1-tdTomato mice (Winters et al., 2012). CB1 BCs revealed strong axonal innervation in deep cortical layers selectively in the V2M, whereas the V1 CB1 interneurons projected mainly within L2/3 (Figures 1D–1F and S2H; relative axonal density: 220 ± 25 and 62 ± 15 vs. 47 ± 20 and 10 ± 6, V2M vs. V1, respectively; n = 7, $p < 0.0001$; Friedman, repeated-measures, post hoc analysis with correction for multiple comparisons, Sidak's multiple comparisons test). Accordingly, CB1 BCs in the V2M exhibited a larger total axonal length than those in the V1 ($p = 0.0379$, Mann–Whitney U test), with no differences in dendritic length in both visual areas ($p = 0.32$, Mann-Whitney U test; Figure 1G).

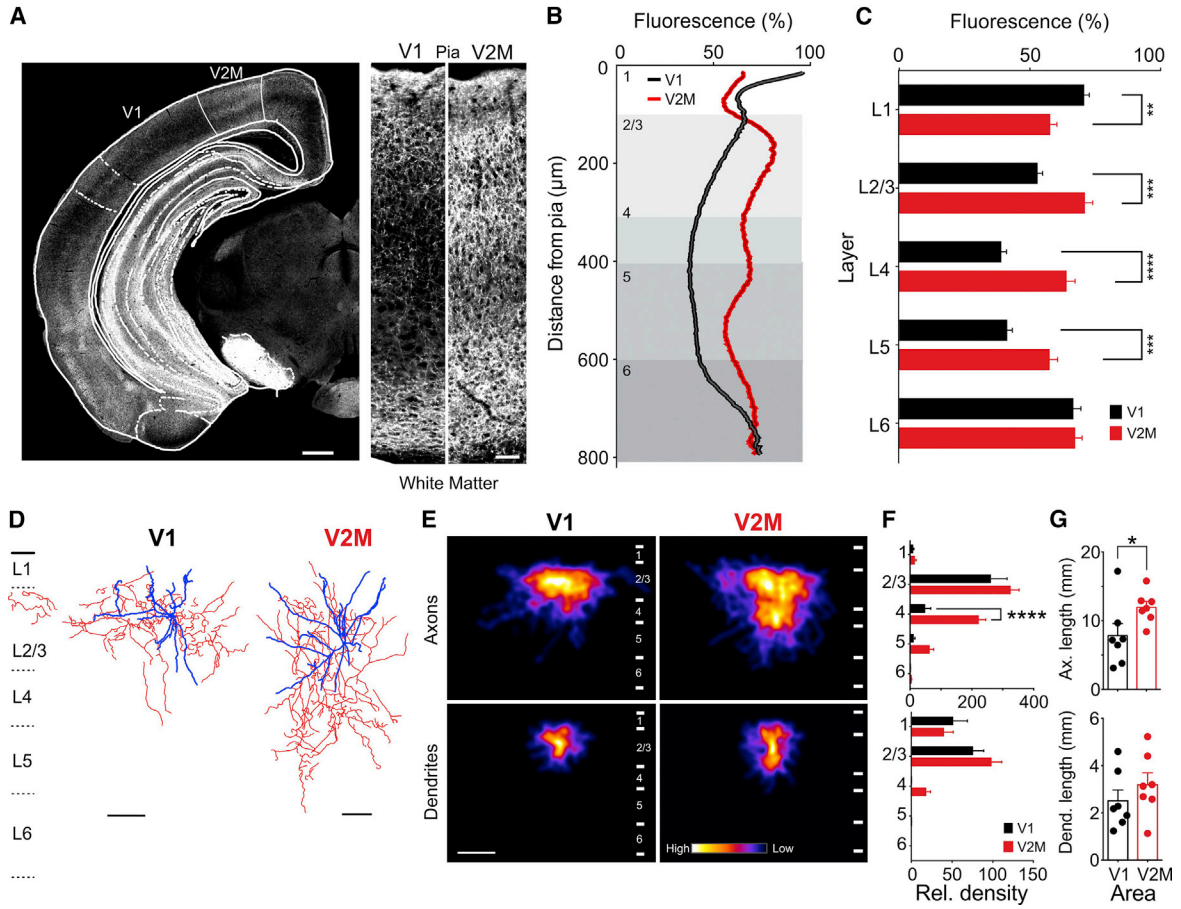

Figure 1. Differential CB1 expression and morphological properties of CB1 interneurons in the V1 and V2M

(A) Left: CB1 immunofluorescence of a coronal mouse brain section, including the V1 and V2M. Scale bar, 500 μm. Right: Magnified side-by-side comparison of CB1 immunofluorescence of the V1 and V2M of the same slice. Scale bar, 50 μm.

(B) Normalized cross-layer CB1 fluorescence intensity in both regions.

(C) Data from (B) binned into cortical layer. **$p < 0.01$, ****$p < 0.0001$; n = 11 animals.

(D) Representative reconstructed CB1 BCs in the V1 (left) and V2M (right). Red, axons; blue, dendrites. Scale bars, 100 μm.

(E) Heatmap of axon and dendrite densities obtained from all filled neurons (n = 7, both areas). Scale bar, 200 μm.

(F) Relative axonal (top) and dendritic (bottom) density, normalized by layer thickness (STAR methods). ****$p < 0.0001$.

(G) Total axonal (top) and dendritic (bottom) length in the two areas. *$p = 0.0379$.

Differences in axonal projection patterns between CB1 BCs in the V1 and V2M could imply different firing signatures. We therefore tested a battery of electrophysiological parameters and found no difference in single action potential waveform and firing dynamics (Figures S3A–S3H).

These results indicate a contrasting pattern of CB1 expression in the V1 and V2M. This is due to more prominent descending axonal innervation selectively in the V2M, suggesting a differential connectivity scheme from this IN subtype in the two visual areas.

Functional differences of intra- and infra-layer connectivity of CB1 BCs in the V1 and V2M

The morphological differences between L2/3 CB1 BCs in the V1 and V2M described above prompts the question of connection probability of CB1 cells within and across layers in the V1 and V2M.

We performed dual simultaneous whole-cell paired recordings between presynaptic CB1 BCs in L2/3 and postsynaptic PNs in L2/3 or L4 in the V1 and V2M (Figures 2A and 2B). In both areas, we reliably obtained connected pairs when the postsynaptic PN was also located in L2/3 (Figure 2A; connected pairs: 56 of 218 versus 53 of 169 in the V1 versus the V2M; $p = 0.38$, Fisher's exact test). However, when the postsynaptic cell was located in L4, the likelihood of obtaining connected pairs was very low in the V1 while remaining high in the V2M (5 of 75 and 46 of 187, respectively; Figure 2A). These connectivity rates are consistent with the axonal morphologies of these cells (Figures 1D–1G). We found that unitary GABAergic responses were ~5.5-fold larger onto PNs in L2/3 of the V1 than the V2M (unitary inhibitory postsynaptic current [uIPSC] amplitude: 183.4 ± 39.93 pA versus 33.38 ± 5.539 pA, L2/3 V1 versus L2/3 V2M, n = 44 and 40, respectively; $p < 0.0001$, Kruskal-Wallis ANOVA followed by Dunn's multiple comparisons test;

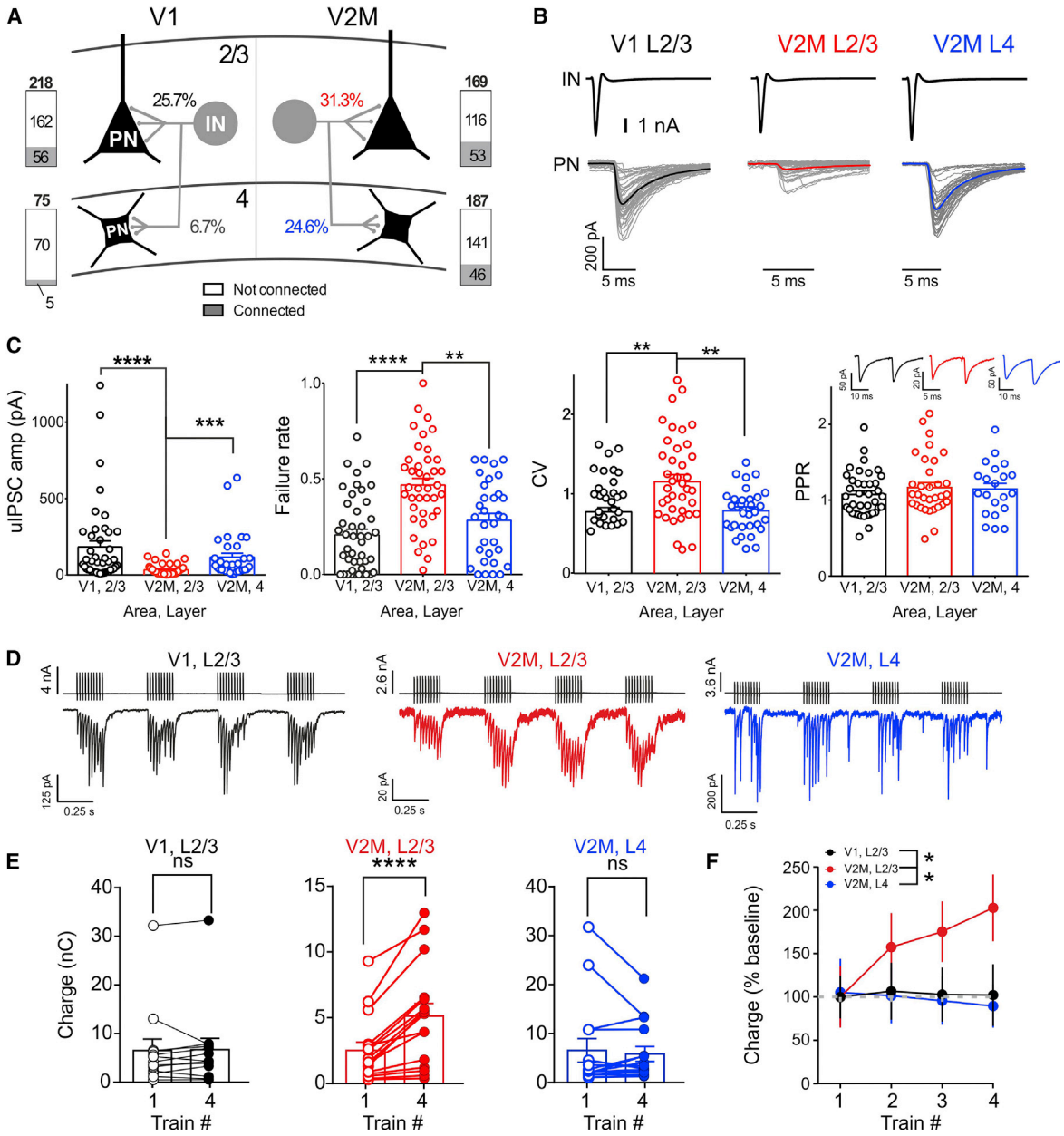

Figure 2. Functional differences of intra- and infra-layer connectivity of CB1 BCs in the V1 and V2M

(A) Connectivity rates of CB1 BCs → PNs within L2/3 and L4 in the V1 and V2M.

(B) Representative uIPSCs in postsynaptic PNs (presynaptic action current above, in black) in V1 L2/3 (average [avg] in black), V2M L2/3 (avg. in red), and V2M L4 (avg. in blue); individual (30) sweeps in light gray.

(C) Population data of uIPSC amplitude, failure rate, coefficient of variation (CV), and paired-pulse ratio (PPR) of the connections illustrated in (B) (same color code).

(D) Representative uIPSCs recorded in PNs in response to four trains of presynaptic action potentials (10 spikes, 50 Hz) in the V1 and V2M (same color code as in B). Shown are averaged traces of at least 10 individual trials.

(E) Population data of total postsynaptic charge, calculated in the first and fourth train.

(F) Population data of percentage change of total postsynaptic charge at the three synapses in the two visual areas. *$p < 0.05$, ****$p < 0.0001$.

Figures 2B and 2C). Accordingly, the failure rate and variability (measured as coefficient of variation [CV]) of uIPSCs were much lower in CB1 IN-PN connections in L2/3 of the V1 than the V2M ($p < 0.0001$ and $p = 0.0028$, respectively; Kruskal-Wallis ANOVA followed by Dunn's multiple comparisons test; Figure 2C). When limiting the analysis to successes only, we did not observe any differences in the paired-pulse ratio (PPR; $p = 0.5$, Kruskal-Wallis ANOVA; Figure 2C). Connected pairs between CB1 BCs and postsynaptic PNs located in L4 of the V2M were stronger and more reliable than connections formed

in L2/3 by the same type of interneurons (L4 uIPSC amplitude: 116.4 ± 26.55 pA, n = 32, p = 0.0013, Kruskal-Wallis ANOVA followed by Dunn's multiple comparisons test; Figure 2C). These infra-laminar connections (from L2/3 to L4 in the V2M) had similar amplitudes, failure rates, and CVs as CB1 IN-PN pairs in L2/3 of the V1 (p > 0.05, Kruskal-Wallis ANOVA for amplitude, failure rate, and CV; Figure 2C). In sum, connections in L2/3 of the V2M were the weakest and most unreliable compared with the neighboring area or layer. When we examined uIPSC rise times (10%–90% rise time), we found that they were fast (<1 ms) and similar for all three synaptic connections (Figure S3I). This is consistent with a perisomatic pattern of innervation, typical of BCs (Figures S3I–S3K).

These data indicate different functional projection patterns in the two visual cortical areas. Inputs from CB1 BCs in the visual cortex exhibit area- and layer-specific properties.

Activity-dependent modulation of synaptic efficacy from CB1 BCs is visual area and layer specific

One of the most prominently studied forms of CB1-dependent GABAergic plasticity is DSI (Castillo et al., 2012). We tested whether CB1-mediated DSI was different in the V1 and V2M. DSI was evoked by 5-s-long postsynaptic depolarizations at 0 mV. We found that CB1-dependent DSI was robustly present in all connected pairs, and it similarly affected uIPSCs in the V1 and V2M in both cortical layers (Figure S4). CB1 signaling can be modulated by presynaptic activity (Lourenço et al., 2014), and GABA release can be persistently modulated by tonic activation of CB1 (Losonczy et al., 2004; Földy et al., 2006; Neu et al., 2007). High-frequency AP trains invading the presynaptic terminal override CB1-mediated tonic modulation of inhibitory transmission (Losonczy et al., 2004; Földy et al., 2006; Neu et al., 2007). We therefore delivered four 50-Hz trains to presynaptic CB1 BCs and found a 2-fold increase in synaptic efficacy (measured as total unitary postsynaptic charge) during train applications only at connections in the V2M between CB1 interneurons and L2/3 PNs (synaptic charge: 2.5 ± 0.6 nC versus 5.1 ± 0.97 nC, train 1 versus train 4; n = 16; p < 0.001, Wilcoxon matched-pairs signed-rank test; Figures 2D–2F). In contrast, in L2/3 of the V1 and in L4 of the V2M, CB1 BC-PN pairs had a similar synaptic charge in response to several presynaptic spike trains (synaptic charge: 6.6 ± 2.3 nC versus 6.7 ± 2.3 nC, train 1 versus train 4, for the V1, L2/3 and 6.6 ± 2.4 nC versus 5.9 ± 1.5 nC, train 1 versus train 4, for the V2M, L4; n = 13 and n = 15, respectively; p = 0.3 for the V1, L2/3 and p = 0.7 for the V2M, L4, respectively; Wilcoxon matched-pairs signed-rank test; Figures 2D–2F).

These results indicate that GABAergic synapses contacting PNs in L2/3 of the V2M were suppressed selectively and persistently. However, this brake could be temporally lifted when presynaptic neurons fired repeatedly.

Visual-area- and layer-specific GABAergic synaptic strength from CB1 BCs is due to selective tonic eBC signaling

The low synaptic efficacy, specific for L2/3 connections at CB1 BC-PN pairs in the V2M, could be due to tonic CB1 signaling. We performed paired recordings in slices pre-incubated with vehicle or the CB1 antagonist AM-251 (3 μM; Figure 3). uIPSC amplitude between connected pairs in V2M L2/3 increased in the presence of AM-251 (uIPSC: 33 ± 6.3 pA versus 148 ± 51 pA, n = 31 versus 15 control versus AM-251; p = 0.0254, Kruskal-Wallis ANOVA followed by Dunn's multiple comparisons test; see below for comparisons with other synapses; Figure 3B), and the failure rate decreased (0.46 ± 0.04 versus 0.25 ± 0.06, n = 31 versus 15 control versus AM-251; p = 0.0059, Mann Whitney test). The CV was not significantly affected by AM-251 treatment (1.2 ± 0.1 versus 0.87 ± 0.1, n = 31 versus 15 control versus AM-251; p = 0.0737, Mann-Whitney test). Our data reveal that antagonizing CB1 converted weak and unreliable connections between CB1 BCs and PNs in L2/3 of the V2M into strong and reliable synapses. In the presence of AM-251, responses elicited in L2/3 of the V2M were similar to those evoked in L2/3 of the V1 and L4 of the V2M (for both synapses, p > 0.99, Kruskal-Wallis ANOVA followed by Dunn's multiple comparisons test). In support of a selective effect in V2M L2/3, the drug had no effect on uIPSCs in the V1, L2/3 and V2M, L4 (V1, L2/3 uIPSC amplitude: 208 ± 46 pA versus 169 ± 49 pA, n = 37 versus 17 control versus AM-251; V2M, L4 uIPSC amplitude: 133 ± 37 pA versus 67 ± 13 pA, n = 22 versus 12 control versus AM-251; p > 0.099, Kruskal-Wallis ANOVA followed by Dunn's multiple comparisons test).

An increase in uIPSC amplitude at L2/3 of V2M GABAergic synapses by AM-251 treatment could reflect ligand-free, persistent CB1 receptor activity, as reported for hippocampal synapses (Losonczy et al., 2004; Földy et al., 2006; Neu et al., 2007; Lee et al., 2010). To test this, we injected viral particles expressing the genetically encoded G protein coupled receptor activation-based (GRAB) eCB sensor GRAB-eCB2.0 to monitor eCB dynamics (Dong et al., 2021; Farrell et al., 2021). We performed 2-photon (2P) eCB imaging in acute cortical slices that included the V1 and V2M. We observed a much stronger decrease in overall fluorescence upon AM-251 application in the V2M than in the V1 (Figure S5). These experiments reveal a stronger tone of eCBs in L2/3 of the V2M compared with the V1. This argues against ligand-free receptor activity as a sole mechanism for the CB1-mediated differential modulation of inhibitory strength in the two cortical areas.

Consistent with young mice, adult (older than post-natal day 60 [P60]) mice exhibited higher CB1 expression, weaker inhibition from CB1 BCs to PNs, and sensitivity to presynaptic repeated activity in the V2M compared with the V1 (Figure S6).

These results indicate that tonic CB1 signaling decreases the strength of GABAergic synapses made by CB1-expressing interneurons selectively in L2/3 of the V2M.

In vivo spontaneous activity of PNs is higher in the V2M compared with the V1

Tonic inhibition of GABA release from CB1 BCs in the V2M should, in principle, result in higher output activity of PNs. To test this hypothesis, we performed *in vivo* 2P Ca^{2+} imaging in awake mice free to locomote on a circular treadmill (Figure 4A). We injected the V1 or V2M with an adeno-associated viral (AAV) vector expressing the genetically encoded Ca^{2+} indicator GCaMP6f under the pan-neuronal promoter synapsin I (*Syn1*), which allowed us to image neuronal activity from putative PNs and tdTomato-expressing CB1 BCs (Figure 4B). We found that the overall mean change in fluorescence ($\Delta F/F_0$) was much higher in the V2M than in the V1 (mean $\Delta F/F_0 = 0.17 \pm 0.02$ versus

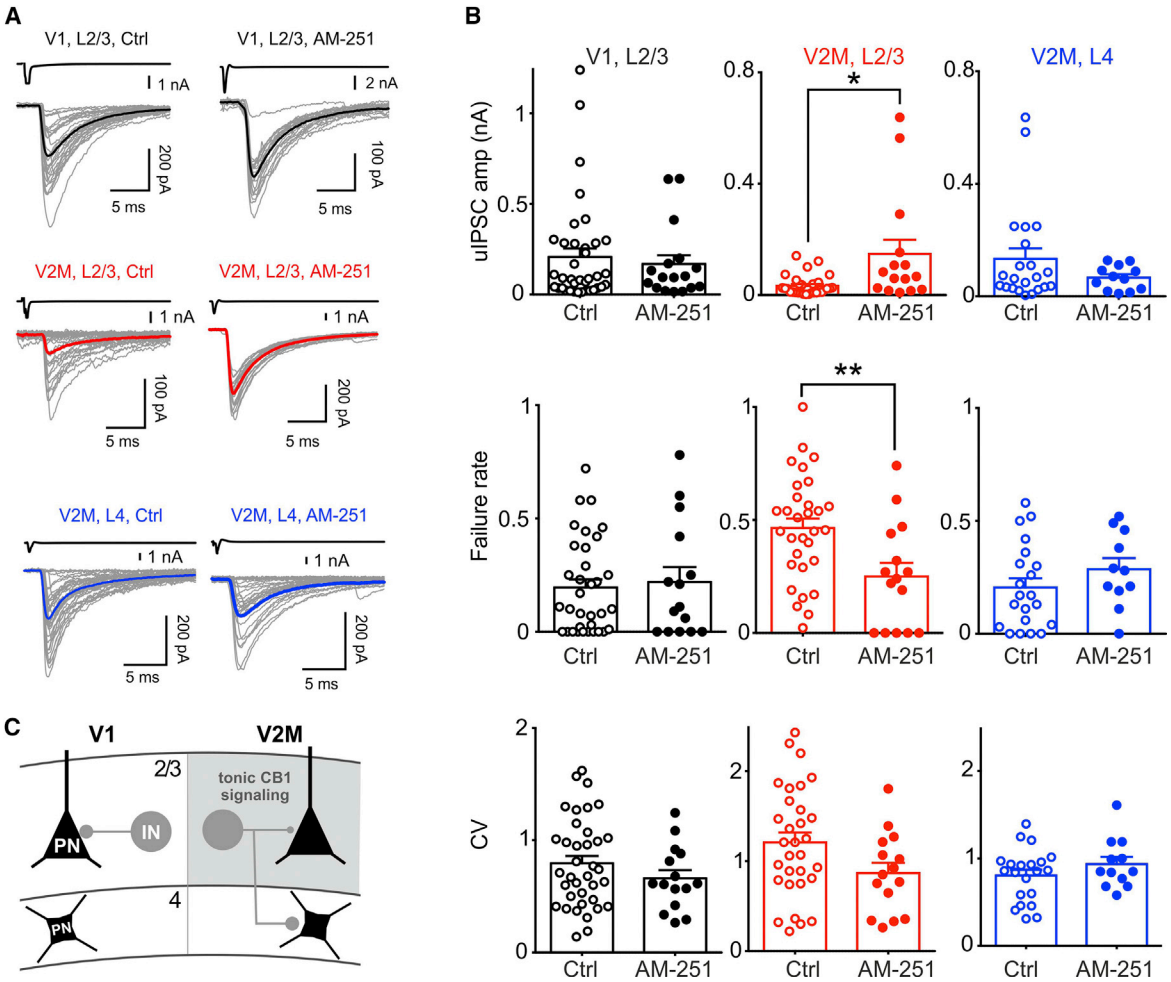

Figure 3. Visual-area- and layer-specific GABAergic synaptic strength from CB1 BCs is due to selective tonic eCB signaling

(A) Representative uIPSC in the absence (control [Ctrl], left) and presence of 3 μM AM-251 (right) in the V1 and V2M. Presynaptic spikes above uIPSCs are shown in black. Gray traces represent individual sweeps.

(B) Population data of uIPSC amplitude (top), failure rate, and CV (bottom) in the control (open symbols) and in the presence of AM-251 (filled symbols).

(C) Schematic summary. The gray area represents the specific expression of tonic CB1 signaling conferring weaker inhibition from CB1 BCs onto PNs in L2/3 of the V2M.

*$p < 0.05$; **$p < 0.01$.

0.31 ± 0.01, V1 versus V2M, respectively; n = 7 and 6 mice in the V1 and V2M, respectively; p = 0.0023; Mann-Whitney U test; Figures 4C and 4D). Higher levels of $\Delta F/F_0$ in the V2M were accompanied by a significant increase in the number of deconvolved events (STAR Methods; Figure S7). We did not find differences in firing dynamics and passive properties between L2/3 PNs of the V1 and V2 (Figures S7C and S7D), ruling out the possibility that higher PN activity in the V2M was due to enhanced intrinsic excitability of PNs in this cortical area.

Higher levels of neuronal $\Delta F/F_0$ in the V2M were not due to differences in movement percentage (21.7% ± 3.5% versus 23.8% ± 0.10% in the V1 and V2M, respectively; p = 0.2949, Mann-Whitney U test; n = 7 and 6 mice in the V1 and V2M, respectively) or speed (0.44 ± 0.06 cm/s versus 0.52 ± 0.09 cm/s in the V1 and V2M, respectively; p = 0.6282, Mann-Whitney U test; n = 7 and 6 mice in the V1 and V2M, respectively) during sampling of V1 or V2M activity. We then restricted our analysis to tdTomato-expressing neurons, and we found that CB1 INs did not exhibit statistically different activity in the two visual areas (mean $\Delta F/F_0$ = 0.27 ± 0.04 versus 0.38 ± 0.04, V1 versus V2M, respectively; n = 7 and 6 mice in the V1 and V2M, respectively; p = 0.10, Mann-Whitney U test; Figures 4E and 4F). This suggests that increased activity in the V2M was overall restricted to PNs.

These results indicate that L2/3 PNs in the V2M fire more than in the V1 under basal conditions.

Visual-area-specific tonic CB1 signaling underlies higher activity in the V2M than V1

To confirm that higher PN activity *in vivo* was due to visual-area-specific tonic CB1 signaling, we injected mice with the specific CB1 inverse agonist SR 141716A (rimonabant; 5 mg/kg intraperitoneally) (Saravia et al., 2017; Compton et al., 1996; Marsicano

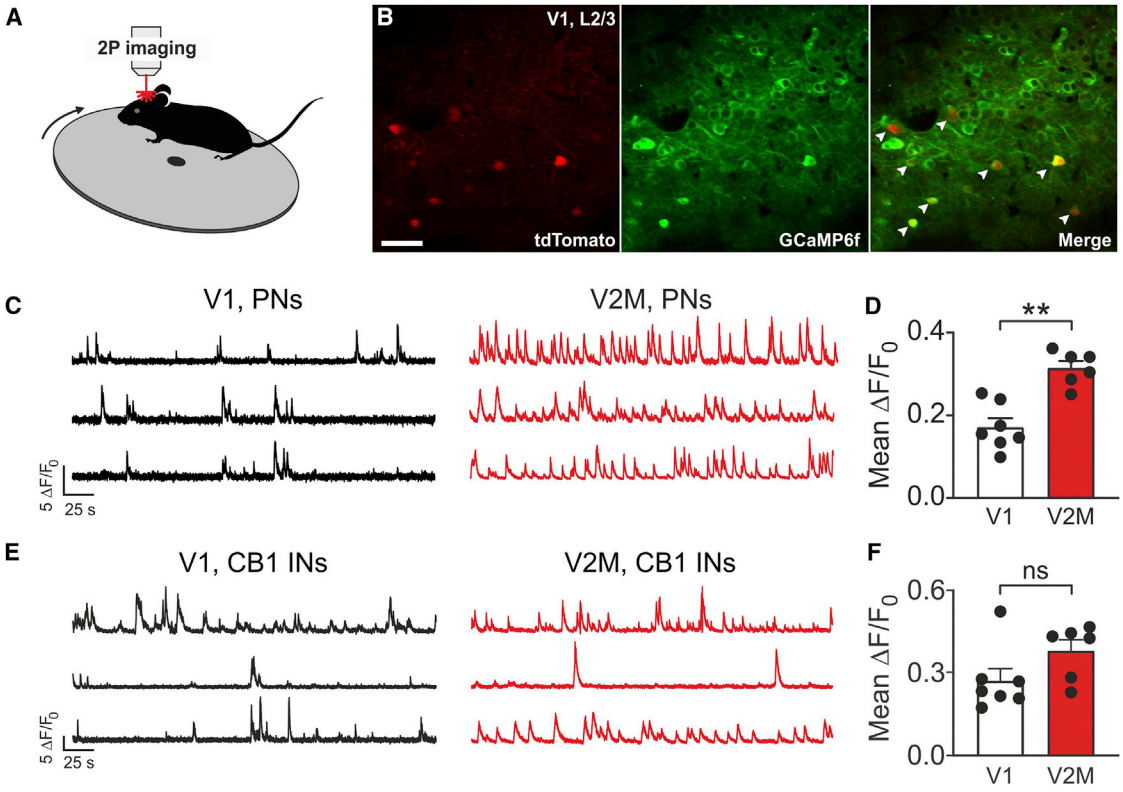

Figure 4. Spontaneous activity of PNs is higher in the V2M compared with the V1

(A) Schematic of 2P Ca^{2+} imaging recordings in awake mice.

(B) Average intensity projection images obtained in L2/3 of the V1 from a CB1-tdTomato mouse. Red, tdTomato expression; green, GCaMP6f expression. Arrowheads point to CB1-expressing neurons. Scale bar, 50 μm.

(C) 2P Ca^{2+} traces from three PNs in the V1 (black, left) and V2M (red, right).

(D) Bar graph of the mean $\Delta F/F_0$ in the V1 (white column) and V2M (red column). Each dot represents an individual mouse. **$p < 0.01$.

(E and F) Same as in (C) and (D) but for tdTomato-expressing interneurons. ns, non-statistically different.

et al., 2002; Rinaldi-Carmona et al., 1994; Varvel et al., 2005). We found that rimonabant did not alter L2/3 neuronal spontaneous activity in the V1 (mean $\Delta F/F_0 = 0.19 \pm 0.03$ versus 0.19 ± 0.05, V1, vehicle versus V1, rimonabant, respectively; n = 6 and 5 mice in the V1, vehicle versus V1, rimonabant, respectively; $p > 0.9999$, Wilcoxon matched-pairs signed-rank test; Figures 5A and 5B). However, the activity of V2M PNs was reduced by ~40% by rimonabant (mean $\Delta F/F_0 = 0.39 \pm 0.06$ versus 0.23 ± 0.04, V2, vehicle versus V2, rimonabant, respectively; n = 6 and 6 mice in V1, vehicle versus V1, rimonabant, respectively; $p = 0.0312$, Wilcoxon matched-pairs signed-rank test; Figures 5A and 5B). These results indicate that the overall higher activity of L2/3 PNs in the V2M was due to CB1 signaling.

Systemic pharmacological blockade does not exclude global CB1 effects. To downregulate CB1 function in adult mice locally in the V1 or V2M, we injected AAVs expressing the recombinase *Cre* under the pCAG promoter in mice carrying a loxP-flanked CB1 gene ($CB1^{floxed/floxed}$) in either cortical area (Soria-Gomez et al., 2014, 2015; Figures 5C and S8). Local genetic knockdown of CB1 did not alter L2/3 PN activity in the V1 (mean $\Delta F/F_0 = 0.11 \pm 0.01$ versus 0.10 ± 0.012, V1-CB1_wild type [WT] versus V1-CB1-knockout [KO], respectively; n = 6 and 5 mice; $p = 0.93$, Mann-Whitney U test; Figures 5D–5F) but strongly reduced the firing of PNs in the V2M (mean $\Delta F/F_0 = 0.49 \pm 0.05$ versus 0.16 ± 0.038, V2M-CB1_WT versus V2M-CB1-KO, respectively; n = 5 and 7 mice; $p = 0.0025$, Mann-Whitney U test; Figures 5D–5F). Similar effects were observed when comparing rates of deconvolved events (Figure S7B).

These results demonstrate the existence of tonic CB1 signaling *in vivo*, which is restricted to the V2M, and that CB1 BCs can exert strong control of PN firing.

Modulation of perisomatic inhibition from CB1 BCs affects correlated activity of PNs selectively in the V2M

Perisomatic inhibition can, in principle, affect the degree of correlated PN activity (Pouille and Scanziani, 2001; Gabernet et al., 2005; Freund and Katona, 2007; Manseau et al., 2010; Buzsaki, 2010; Lourenço et al., 2014, 2020a). We therefore extracted the relative timing of the deconvolved events between PNs in our 2P imaging experiments and quantified pairwise correlations of PNs in the V1 and V2M. We measured the spike time tiling coefficient (STTC) of deconvolved events to reduce possible confounding effects linked to differences in firing rates (STAR Methods; Cutts and Eglen, 2014). We found that neurons

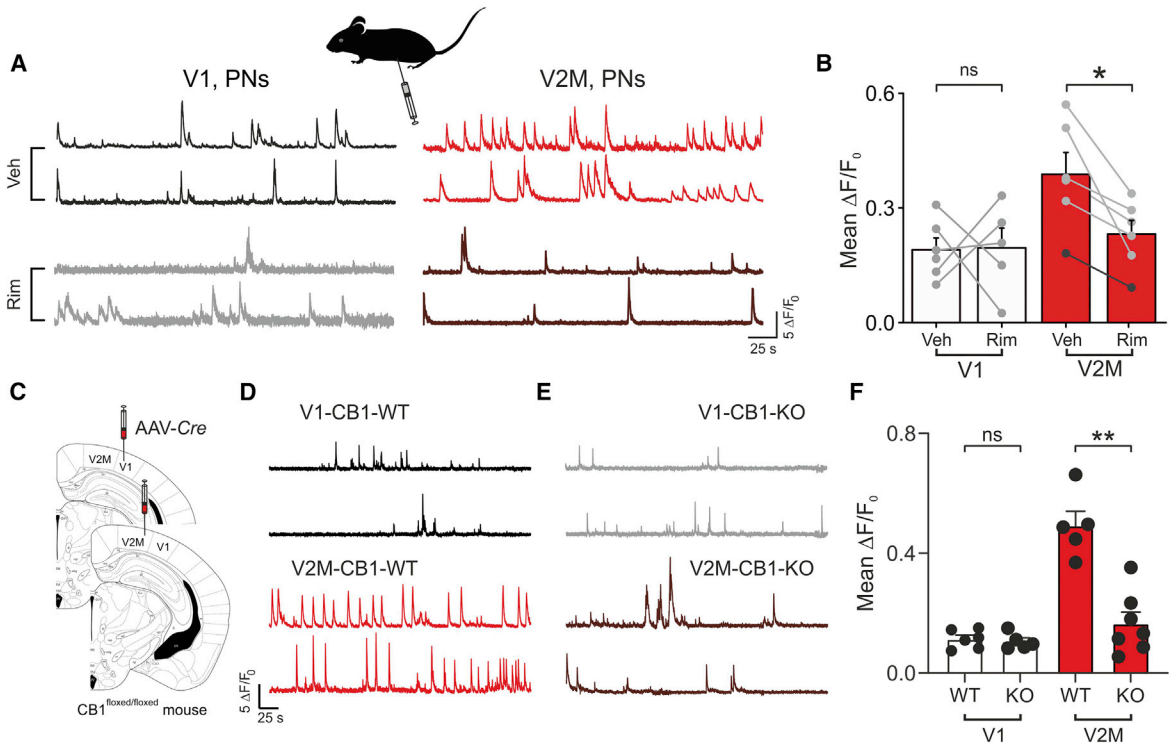

Figure 5. Visual area-specific tonic CB1 signaling underlies higher activity in the V2M than V1

(A) 2P Ca^{2+} traces from two PNs in the V1 (black, left) and V2M (red, right) in two control mice injected with vehicle solution (top) and with the CB1 antagonist rimonabant (bottom).

(B) Bar graph of the mean $\Delta F/F_0$ in the V1 (white columns) and V2M (red columns) for vehicle- and rimonabant-injected mice. Each gray dot represents an individual mouse. The darker dot refers to a $CB1^{floxed/floxed}$ mouse.

(C) Schematic of local genetic CB1 deletion in the two visual areas using adult $CB1^{floxed/floxed}$ mice with AAV-*Cre* or control (AAV-tdTomato) vectors injected into the V1 or V2M.

(D) Ca^{2+} activity from two PNs in the V1 injected with the control AAV (V1-CB1-WT, top) and AAV-*Cre* (V1-CB1-KO) vectors (bottom).

(E) Same as in (D) but for the V2M.

(F) Bar graph illustrating the mean $\Delta F/F_0$ in the V1 (white columns) and V2M (red columns) for mice (black dots) injected with control or *Cre* vectors.

*$p < 0.05$; **$p < 0.01$; ns, non-statistically different.

in the V2M (characterized by higher activity) exhibited less correlated activity of deconvolved events compared with the V1 (STTC: 0.06 ± 0.004 versus 0.05 ± 0.004, V1 versus V2M; n = 70 and 62 time series; p = 0.033, Mann-Whitney U test; Figures 6A and 6B). STTC analysis revealed a significant proportion of cells in the V1 and V2M with coordinated activity above chance levels (Figure S9; STAR Methods).

Genetic CB1 deletion in the V1 did not affect STTC (STTC: 0.07 ± 0.01 versus 0.01 ± 0.03, V1-CB1-WT versus V1-CB1-KO; n = 29 and 24 time series; p = 0.67, Mann-Whitney U test; Figures 6C and 6D). In contrast, knocking out CB1 in the V2M resulted in a significant increase in correlated activity in this visual area (STTC: 0.04 ± 0.005 versus 0.08 ± 0.02, V2M-CB1-WT versus V2M-CB1-KO; n = 27 and 33 time series; p = 0.023, Mann-Whitney U test; Figures 6E and 6F).

These data indicate that CB1 BCs contribute significantly to orchestrate cortical networks. More strikingly, these results indicate that tonic CB1 signaling is a simple, albeit powerful mechanism to control the level of activity and coordination of PNs in different cortical areas.

A computational network model incorporating visual-area-specific circuit properties captures the differential firing dynamics in the V1 and V2M

Spontaneous behavior is the main source of correlated activity in the sensory (including visual) cortex (McGinley et al., 2015; Niell and Stryker, 2010; Stringer et al., 2019), and it increases PN activity, partly because of thalamic activity (Busse et al., 2017; Dipoppa et al., 2018; Saleem et al., 2013; Saleem, 2020; Nestvogel and McCormick, 2022; Poulet et al., 2012). Accordingly, we found that PN activity was strongly modulated by locomotion (Figure S10). Pairwise spiking correlations, resulting from shared input, should increase monotonically with firing rates (de la Rocha et al., 2007). However, we found that PNs in the V2M fired less synchronously than in the V1 (Figure 6). It is possible that the specific feedback-inhibitory loop from L4 (Figure 2) is involved in controlling correlated activity in V2M firing rate, along with CB1 tonic signaling. To test this hypothesis, we generated a spiking network model characterized by different properties in the CB1 BC population in terms of connectivity and release probability (STAR Methods; Figures 7A–7C).

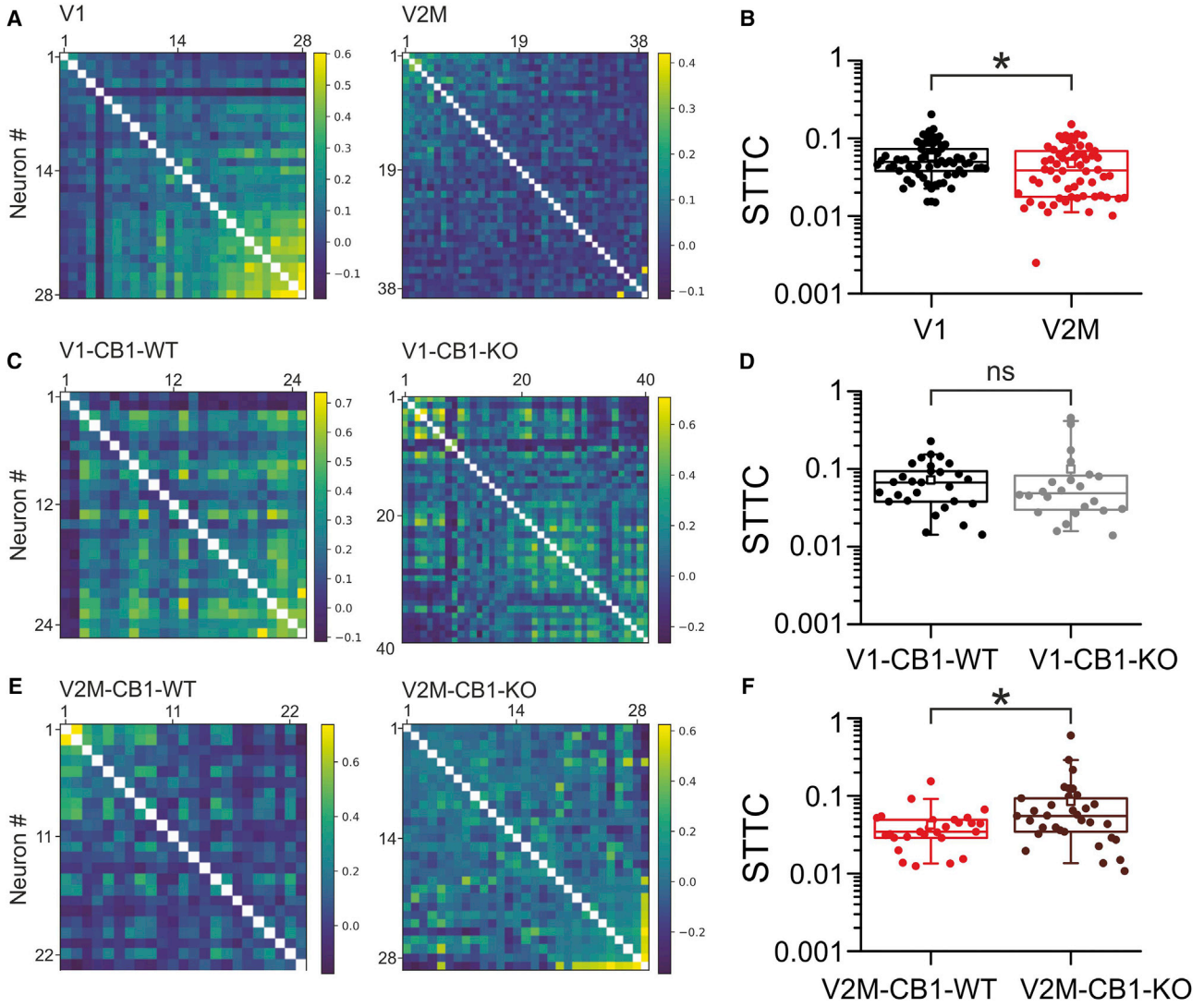

Figure 6. Modulation of perisomatic inhibition from CB1 BCs affects correlated activity of PNs selectively in the V2M

(A) Pairwise correlation matrices of a recording session in the V1 (left) and V2M (right). The heatmaps indicate levels of correlated activity (STTC, spike time tiling coefficient).

(B) STTC in the V1 (black) and V2M (red). Each dot represents a time series.

(C–F) Same as in (A) and (B) but for CB1$^{floxed/floxed}$ mice injected with control AAV (CB1-WT) and AVV-Cre (CB1-KO) vectors in the V1 (C and D) and V2M (E and F). The color code for different viral vectors and visual areas in (D) and (F) is as in Figure 5D.

*$p < 0.05$

We analyzed the stationary activity of the cortical network resulting from different release probabilities at CB1 BC-PN synapses, mimicking V2M-specific CB1-mediated tonic modulation of GABA release (Figures 7A–7C). In a V1-like scenario, more reliable GABA release from CB1 BCs yielded overall reduced activity in all cell types (Figures 7D–7F), explaining the lower activity of V1 L2/3 PNs compared with the V2M that we recorded experimentally (Figures 4 and 5). Removing the CB1 control of GABA release reduced the spontaneous activity of a V2M-like network (V2M-CB1-KO; Figures 7D–7F).

We then introduced random waveform stimulation of L4 that depolarized L4 PNs more strongly in the V1 (Figure 7G), yielding a combined positive gain of the L2/3 and L4 networks (Figures S11 and 7G). This led to recurrent amplification of the input signal and created positive correlations in the network (Figure 7I). In the V2M case, despite higher excitability of the L2/3 network with respect to the V1 (Figure S11), the presence of the inhibitory feedback L4 loop by CB1 BCs prevented depolarization of L4 PNs and reduced the input-output gain of L4 (Figure S11) and of the overall L4-L2/3 networks (Figure 7H). The ratio between evoked and spontaneous activity was drastically reduced (Figure 7I), and spontaneous activity (a regimen of near-zero correlations; STAR Methods) provided a much higher contribution to average spiking correlations. Consequently, V2M neurons had lower correlated activity than the V1

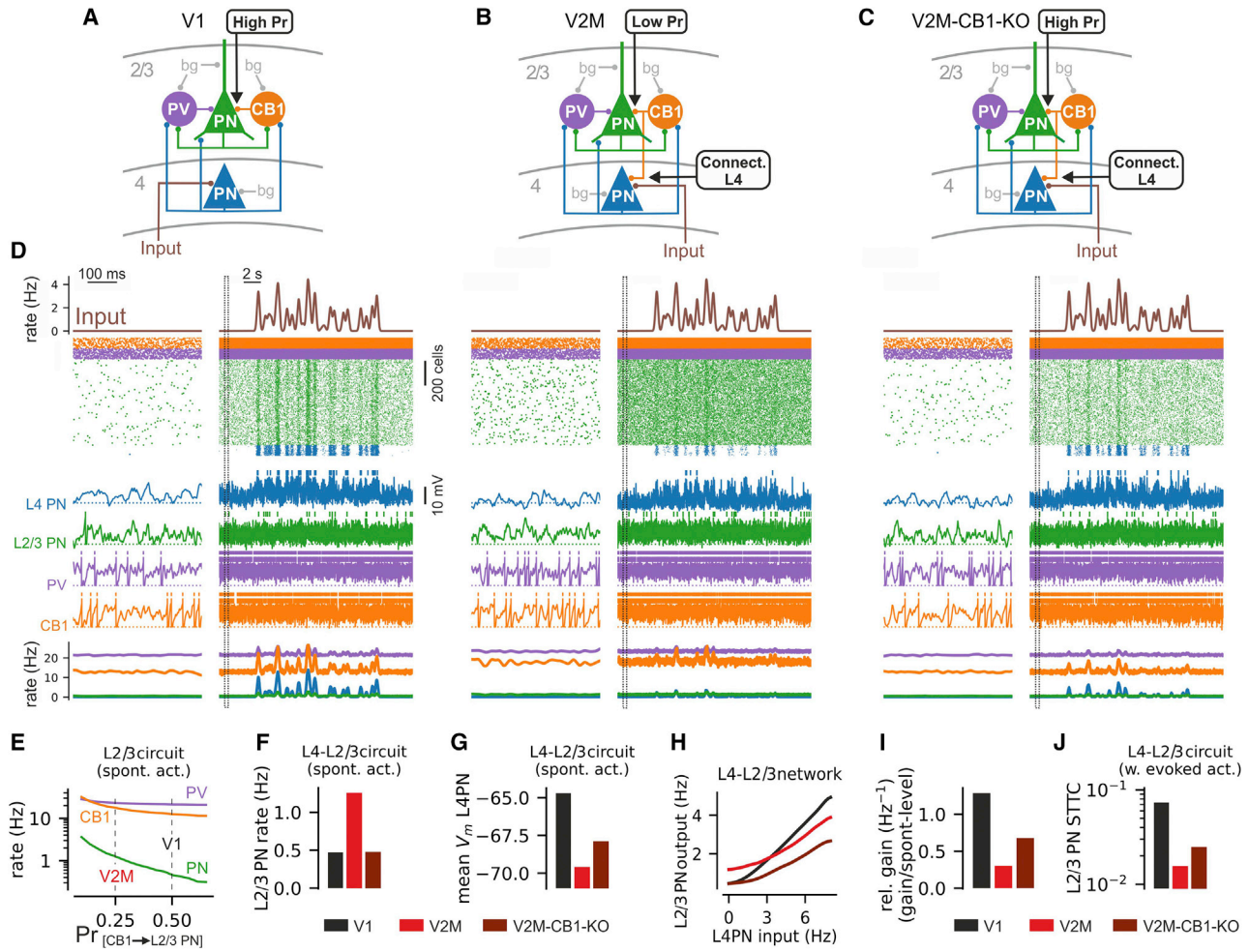

Figure 7. Computational modeling of the effect of the visual-area-specific CB1 modulation properties on the dynamics of cortical circuits

(A–C) Schematic of the network models for the L4-L2/3 circuits in the V1 (A), V2M (B), and V2M-CB1-KO (C).

(D) Single realizations of the network simulations. Shown is spike raster activity of CB1 (orange), PV (purple) BCs, L2/3PNs (green), and L4 PNs (blue) at two different time scales. Example V_m traces and the time-varying rates for each neuronal population are shown. Spiking events are truncated for display. Input to L4 is shown at the top (brown). V1, left; V2M, center; V2M-CB1-KO, right.

(E) Spontaneous firing rates as a function of release probability in the three cases.

(F) Spontaneous activity rates of L2/3 PNs in the 3 cases of (A)–(C).

(G) Mean depolarization of L4 PNs during spontaneous activity in the 3 cases of (A)–(C).

(H) L4 input to L2/3 output curves in the 3 cases of (A)–(C).

(I) Gain of the spontaneous activity levels in the 3 cases shown in (A)–(C). This quantity reflects the ratio of evoked and spontaneous activity in the network.

(J) 300-ms STTC for the simulation shown in (A)–(C).

model (Figure 7J; STTC in the V1 versus V2M: 0.078 ± 0.021 versus 0.017 ± 0.003, p = 9e−12, paired t test, n = 20 seeds).

When we removed the CB1 modulation at the L2/3 PN synapses while keeping intact the inhibitory feedback from CB1 BCs to L4 PNs (mimicking V2M-CB1-KOs; Figure 7C), we observed partial recovery of pairwise correlations in the network (Figure 7I; STTC in V2M-CB1-KO versus V2M: 0.023 ± 0.007 versus 0.017 ± 0.003, paired t test, p = 6e−4, n = 20 seeds).

Overall, the present model recapitulates our experimental findings and proposes a mechanism by which CB1-mediated modulation of GABA release from this BC subtype regulates firing rate and network coordination across cortical areas.

DISCUSSION

In this study, we examined the functional connectivity pattern of CB1 BCs in the mouse visual cortex in slices and *in vivo*. CB1 BCs are elusive elements of the cortical microcircuit, and their functional properties are much less known compared with other inhibitory cell types, such as dendritic targeting somatostatin (SST) and perisomatic PV interneurons. We found that CB1 expression was higher in the V2M across L2–L5 compared with the V1. We also found that CB1-expressing BCs possessed different anatomical and connectivity patterns in the V1 versus V2M. Overall, CB1 BCs in L2/3 of the V2M had much lower

efficacy of synaptic release because of persistently active CB1 signaling in this specific layer and cortical visual area (Figure 3C). Our *in vivo* data and numerical simulations indicate that area-specific connectivity and eCB modulation can contribute to higher but less coordinated activity of PNs in the V2M compared with the V1.

The V2M-specific infra-laminar projection of CB1 BCs indicates the existence of specific circuit motifs in different cortical areas (but see Eggan et al., 2010). This heterogeneous distribution might be preserved in the adult central nervous system (Glass et al., 1997). L4 activation by thalamo-cortical fibers is relayed to L2/3, where it may generate a feedback-inhibitory loop operated by CB1 BCs only in associative cortices. Our numerical simulations reveal that the inhibitory feedback loop involving CB1 BC projections to L4 can account for the counter-intuitive reduction of L2/3 PN coordination in a higher-frequency regimen. Thus, this associative area-specific routing of intracortical information could have important consequences for sensory perception.

Differences in anatomical parameters, such as dendritic and axonal projections, have traditionally been used to distinguish different interneuron subclasses (Markram et al., 2004; Ascoli et al., 2008; Naka et al., 2019). Accordingly, different morphologically identified cell types exhibit specific electrophysiological properties (Markram et al., 2004). Here we found that, despite the different axonal projections in the two visual areas, CB1 BCs exhibited a similar electrophysiological signature. GABAergic synaptic transmission from CB1 BCs has many similarities in the two visual areas, such as a high failure rate and variable short-term dynamics, consistent with their counterparts in the hippocampus (Hefft and Jonas, 2005; Neu et al., 2007; Daw et al., 2009), amygdala (Rovira-Esteban et al., 2017), and other cortical areas (Galarreta et al., 2008). This argues against the existence of distinct subtypes of cortical CB1 BCs in different visual areas, although a thorough molecular investigation using single-cell transcriptomics will be important to pinpoint possible selective expression profiles. Importantly, however, GABAergic transmission was much weaker onto L2/3 PNs of the V2M, but this layer- and visual-area-specific synaptic efficacy was erased by blocking CB1 receptors (CB1Rs). This indicates that the different inhibitory strength exhibited in L2/3 of the V2M did not depend on the specificity of pre- and postsynaptic molecular architecture (Eggermann et al., 2011) was due to persistent modulation of GABA release from CB1 BCs only in this layer of this associative visual area, resulting in functional synaptic diversity and target specificity.

Despite an increase in uIPSC amplitude and a decrease in failure rate, the lack of change in PPR in the presence of AM251 is unexpected but also consistent with other studies (Kim and Alger, 2001; Rovira-Esteban et al., 2017). Thus, PPRs with two consecutive IPSCs may not be an appropriate measure of presynaptic release probability at these synapses. Using PPR to infer the presynaptic release probability of GABAergic synapses has been questioned in the hippocampus because of spurious facilitation caused by occasional synaptic failure (Kim and Alger, 2001; Hefft et al., 2002; Burke et al., 2018). However, AM-251 application decreased the uIPSC failure rate, consistent with presynaptic modulation by CB1 (Neu et al., 2007).

Irrespective of selective tonic CB1 modulation, CB1-dependent DSI magnitude was similar at the three tested connections. This indicates that tonic CB1 signaling in the V2M does not saturate the receptor, which is still sensitive to depolarization-induced, on-demand production of eCBs. However, although the relative DSI amplitude was similar in the V1 and V2M, it is important to stress here that, from the perspective of single PNs, DSI produced a massive reduction of PN perisomatic inhibition in L2/3 of the V1 (synaptic currents went from several hundred pA to zero). In contrast, L2/3 PNs of the V2M sensed a reduction of perisomatic inhibition from CB1 INs, which was already weak (~6-fold less powerful) already before DSI stimuli. This differential absolute change of acute eCB modulation of inhibitory transmission from CB1 interneurons will likely produce distinct effects in the output spiking properties of single PNs in the two cortical areas.

CB1-dependent tonic reduction of inhibition has been reported at GABAergic synapses in the hippocampus (Losonczy et al., 2004; Földy et al., 2006; Neu et al., 2007), although the existence of tonic CB1 signaling is disputed (Castillo et al., 2012). This has raised the possibility that tonic inhibition could depend on the health of the slice preparation and/or recording conditions. Here we demonstrate in adult tissue that the same CB1 neuron could be responsible for phasic and tonic modulation at different synapses. We found that tonic CB1 modulation had a strong effect on modulating *in vivo* PN firing behavior selectively in the V2M.

Tonic CB1 activation could be due to different mechanisms, including a constitutively active receptor in the absence of a natural ligand (Leterrier et al., 2004; Losonczy et al., 2004) or a persistently activated receptor by a tonic presence and/or synthesis of eCBs (Neu et al., 2007; Lee et al., 2015). Our eCB imaging data suggest a stronger tone of endogenous ligands in L2/3 of the V2M compared with the V1. Such a finding argues against a ligand-free receptor activity as the unique mechanism underlying tonic silencing of CB1-expressing GABAergic synapses. The possible sources of eCBs remain to be elucidated and could include non-neuronal elements in the neuropil (such as astrocytes). Alternatively, tonic CB1 activation could derive from layer-specific reduced expression of enzymatic eCB degradation machinery (Ladarre et al., 2014). Finally, that the higher ambient eCB concentration could be due to elevated activity of PNs in the V2M is unlikely because PNs were equally quiescent in the two visual areas in acute slices.

Independent of the actual underlying molecular mechanism, it has been shown that tonic CB1 activity can be overrun by high-frequency firing of presynaptic interneurons (Chen et al., 2003, 2007; Földy et al., 2007), or it could be facilitated by presynaptic activity (Zhu and Lovinger, 2007; Heifets et al., 2008; Lourenço et al., 2010). Here we show that the strength of CB1-mediated modulation of GABA release onto PNs can be modulated by the firing activity of presynaptic CB1 BCs. Maturation of the visual cortex and stress conditions could alter CB1 expression and, thus, be factors altering CB1 signaling (Jiang et al., 2010; Wamsteeker Cusulin et al., 2014). We found that the visual-area-specific expression of CB1Rs and consequent differential strength of CB1-sensitive perisomatic inhibition was also present in adult (>P60) mice. This rules out the possibility that tonic CB1 modulation of GABA release is specific for juvenile mice, in which cortical circuits are still undergoing experience-dependent maturation.

Weak perisomatic inhibition in the V2M might be used as a strategy to modulate postsynaptic PN firing. We observed much higher spontaneous *in vivo* activity of PNs in this associative area as opposed to the V1. This is consistent with overall decreased inhibition onto PNs. In sensory cortices, L2/3 PNs exhibit low-frequency activity, suggesting that they integrate sensory input using sparse coding (Petersen and Crochet, 2013). We found a stark difference of activity of L2/3 PNs in adjacent visual cortical areas. One can thus speculate that higher-order visual cortical regions encode sensory information using a different computational strategy. Future experiments will define the actual role of this difference in firing in the hierarchical flow of sensory information involving primary and associative cortical areas (Glickfeld and Olsen, 2017; Minderer et al., 2019; Jin and Glickfeld, 2020; Siegle et al., 2021).

Is this visual area-specific PN activity level dependent on the strength of GABAergic neurotransmission onto PNs? In particular, do CB1 BCs contribute to set the activity level of PNs in different cortical areas? We found that pharmacological blockade and genetic deletion of CB1 reduced the activity of PNs in the V2M to levels similar to that in the V1. The decrease in neuronal activity observed in the V2M after pharmacological CB1 blockade could be ascribed to a brain-wide or even peripheral effect. However, the virtually identical results were obtained by acute and localized genetic deletion of CB1 in the V1 or V2M in adult mice, strengthening our interpretation that this difference in neuronal activity is due to tonic CB1 signaling. This result strongly suggests that CB1 INs control the output activity of PNs. This result reveals the presence of tonic CB1 signaling in a specific cortical area (V2M), in good agreement with our anatomical and synaptic findings (Figures 1, 2, and 3).

The difference in PN firing in the V1 and V2M was not associated with significant firing alterations of CB1 INs. This suggests that these cells are likely poorly recruited by local PNs, which exhibit higher activity in the visual areas. The lack of difference in firing frequency between CB1 INs in the V1 and V2M suggests functional decoupling between their firing behavior and synaptic release of GABA. The overall spontaneous activity of CB1 INs may not be sufficient to overcome tonic CB1 inhibition of GABA release.

Perisomatic inhibition controls the timing and synchronization of PN firing. In addition, the level of correlated activity increases along with the firing rate (de la Rocha et al., 2007; Renart et al., 2010). Intriguingly, we observed a lower synchrony in the V2M in the presence of higher firing activity. Our network model considers area-specific CB1 properties on inhibitory neurotransmission affecting neural network dynamics during spontaneous activity and in response to an external stimulus. The model well captures the differential coordination of PN activity, induced by tonic reduction of GABAergic inhibition from CB1 BCs in the V1 and V2M. In this model, we also considered inhibition from PV cells. The model predicts that the combination of decreased probability of GABA release from CB1 BCs in the V2M and their inhibitory feedback loop to L4 PNs accounts for the counter-intuitive reduction of L2/3 PN coordination in a higher-frequency firing regimen. Future experiments will be necessary to unravel the actual synchronization role played by CB1 BCs, with a better temporal resolution, to reveal whether these BCs are involved in fast network oscillations, as shown in the hippocampus (Hajos et al., 2000; Robbe et al., 2006).

The highly specific inhibitory modulation of PN output can profoundly affect the participation and orchestration of populations of PNs to relevant network oscillations, proposed to underlie several cognitive functions, including sensory perceptions (Buzsaki, 2010; Siegle et al., 2014). It has been shown recently that hippocampal CCK/CB1 and PV BCs play a complementary role during fast network activity because of mutual inhibitory connections between these IN subclasses (Dudok et al., 2021). Whether this scheme applies also to different visual cortical areas and whether visual stimuli can affect this functional connectivity (Dipoppa et al., 2018) is not known. It is tempting to speculate that, given our effect of CB1 tonic modulation selectively in the V2M, perisomatic inhibition from CB1 BCs plays a predominant role in this specific cortical area.

We found that different morpho-functional and connectivity properties of a specific GABAergic IN subtype governs the activity level of a visual cortical area, suggesting that distinct circuit blueprints can define the function of specific cortical areas during sensory perception.

Limitations of the study

Because all *in vivo* experiments used 2P Ca^{2+} imaging approaches, electrophysiological recordings from awake mice could have provided a better temporal resolution to study correlated activity patterns across different visual areas and unravel the actual synchronization role played by CB1 BCs. Likewise, simultaneous recordings of the V1 and V2M brain areas in the presence of visual stimulation would have given precious insights into the role of tonic CB1 during visual perception.

STAR★METHODS

Detailed methods are provided in the online version of this paper and include the following:

- KEY RESOURCES TABLE
- RESOURCE AVAILABILITY
  - Lead contact
  - Materials availability
  - Data and code availability
- EXPERIMENTAL MODEL AND SUBJECT DETAILS
  - Animals
- METHOD DETAILS
  - Immunohistochemistry and cell counting
  - CB1 immunofluorescence pattern
  - Combined fluorescent *in situ* hybridization (FISH)/Immunohistochemistry (IHC) on free-floating frozen sections
  - Counting CB1 INs
  - In vitro slice preparation for electrophysiological recordings
  - Electrophysiology
  - Morphological reconstruction
  - Two-photon imaging of eCB in acute mouse brain slices

SUPPLEMENTAL INFORMATION

Supplemental information can be found online at https://doi.org/10.1016/j.celrep.2022.111202.

ACKNOWLEDGMENTS

We thank Brahim Abbes for providing the Fiji plugin (Neurostack) for soma co-localization analysis and quantification and Ronan Chéreau and Michael Graupner for initial help with 2P imaging implementation. We also thank members of the Bacci laboratory for helpful discussions and the ICM technical staff of the facilities PHENO-ICMICE, iGENSEQ, and Histomics. All animal work was conducted at the PHENO-ICMice facility. We gratefully acknowledge Joanna Droesbeke for performing part of the transcardial perfusions. F.K. thanks the Fondation des Treilles for awarding her the 2020 Young Researchers Prize. This work was supported by "Investissements d'avenir" ANR-10-IAIHU-06, Agence Nationale de la Recherche (ANR-13-BSV4-0015-01, ANR-16-CE16-0007-02, ANR-17-CE16-0026-01, ANR-18-CE16-0011-01, and ANR-20-CE16-0011-01), Fondation pour la Recherche Médicale (Equipes FRM – DEQ20150331684, Equipes FRM – EQU201903007860), DIM Region Ile de France, and a grant from the Institut du Cerveau et de la Moelle épinière (Paris) (to A.B.); European Research Council (starting grant 678250) and the Brain & Behavior Research Foundation (NARSAD Young Investigator Grant) (to N.R.); Fondation pour la Recherche Médicale (ARF 201909009117) (to Y.Z.); the German Research Foundation through the Cluster of Excellence (EXC2067) Multiscale Imaging and the Collaborative Research Center 889 (project B3) (to O.M.S.). The Core ICM facilities were supported by 2 "Investissements d'avenir" (ANR-10- IAIHU-06 and ANR-11-INBS-0011-NeurATRIS) and the "Fondation pour la Recherche Médicale". This project has received funding from the European Union's Horizon 2020 research and innovation program under Marie Skłodowska-Curie grant agreement 892175 (to Y.Z.).

AUTHOR CONTRIBUTIONS

F.K., M.M., A.B., and J.L. designed the research. F.K., M.M., A.A., J.P., M.V., F.J.-K., C.A., P.M., and J.L. collected data. M.M., F.K., A.A., J.P., and J.L. analyzed data. V.C., M.D.B.V.V., N.R., and A.B. provided analytical tools. G.M. and O.M.S. provided CB1 mouse lines and viral vectors. Y.Z. performed the network modeling work with critical feedback from N.R., F.K., A.B., and J L. A.B. and J.L. co-supervised the project. F.K., M.M., A.B., and J.L. wrote the manuscript. All authors edited the manuscript.

DECLARATION OF INTERESTS

The authors declare no competing interests.

Received: September 3, 2021
Revised: May 24, 2022
Accepted: July 21, 2022
Published: August 23, 2022

REFERENCES

Allene, C., Lourenço, J., and Bacci, A. (2015). The neuronal identity bias behind neocortical GABAergic plasticity. Trends Neurosci. *38*, 524–534.

Ascoli, G.A., Alonso-Nanclares, L., Anderson, S.A., Barrionuevo, G., Benavides-Piccione, R., Burkhalter, A., Buzsaki, G., Cauli, B., DeFelipe, J., Fairen, A., et al. (2008). Petilla terminology: nomenclature of features of GABAergic interneurons of the cerebral cortex. Nat. Rev. Neurosci. *9*, 557–568.

Atallah, B.V., Bruns, W., Carandini, M., and Scanziani, M. (2012). Parvalbumin-expressing interneurons linearly transform cortical responses to visual stimuli. Neuron *73*, 159–170.

Armstrong, C., and Soltesz, I. (2012). Basket cell dichotomy in microcircuit function. J. Physiol. *590*, 683–694.

Bellocchio, L., Soria-Gómez, E., Quarta, C., Metna-Laurent, M., Cardinal, P., Binder, E., Cannich, A., Delamarre, A., Häring, M., Martín-Fontecha, M., et al. (2013). Activation of the sympathetic nervous system mediates hypophagic and anxiety-like effects of CB_1 receptor blockade. Proc. Natl. Acad. Sci. USA *110*, 4786–4791.

Bodor, A.L., Katona, I., Nyíri, G., Mackie, K., Ledent, C., Hájos, N., and Freund, T.F. (2005). Endocannabinoid signaling in rat somatosensory cortex: laminar differences and involvement of specific interneuron types. J. Neurosci. *25*, 6845–6856.

Bortone, D.S., Olsen, S.R., and Scanziani, M. (2014). Translaminar inhibitory cells recruited by layer 6 corticothalamic neurons suppress visual cortex. Neuron *82*, 474–485.

Burke, K.J., Jr., Keeshen, C.M., and Bender, K.J. (2018). Two forms of synaptic depression produced by differential neuromodulation of presynaptic calcium channels. Neuron *99*, 969–984.e7.

Busse, L., Cardin, J.A., Chiappe, M.E., Halassa, M.M., McGinley, M.J., Yamashita, T., and Saleem, A.B. (2017). Sensation during active behaviors. J. Neurosci. *37*, 10826–10834.

Buzsáki, G. (2010). Neural syntax: cell assemblies, synapsembles, and readers. Neuron *68*, 362–385.

Buzsáki, G., and Wang, X.J. (2012). Mechanisms of gamma oscillations. Annu. Rev. Neurosci. *35*, 203–225.

Castillo, P.E., Younts, T.J., Chavez, A.E., and Hashimotodani, Y. (2012). Endocannabinoid signaling and synaptic function. Neuron *76*, 70–81.

Chen, K., Neu, A., Howard, A.L., Földy, C., Echegoyen, J., Hilgenberg, L., Smith, M., Mackie, K., and Soltesz, I. (2007). Prevention of plasticity of endocannabinoid signaling inhibits persistent limbic hyperexcitability caused by developmental seizures. J. Neurosci. *27*, 46–58.

Chen, K., Ratzliff, A., Hilgenberg, L., Gulyás, A., Freund, T.F., Smith, M., Dinh, T.P., Piomelli, D., Mackie, K., and Soltesz, I. (2003). Long-term plasticity of endocannabinoid signaling induced by developmental febrile seizures. Neuron *39*, 599–611.

Clancy, K.B., Orsolic, I., and Mrsic-Flogel, T.D. (2019). Locomotion-dependent remapping of distributed cortical networks. Nat. Neurosci. *22*, 778–786.

Compton, D.R., Aceto, M.D., Lowe, J., and Martin, B.R. (1996). In vivo characterization of a specific cannabinoid receptor antagonist (SR141716A): inhibition of delta 9-tetrahydrocannabinol-induced responses and apparent agonist activity. J. Pharmacol. Exp. Ther. *277*, 586–594.

Cutts, C.S., and Eglen, S.J. (2014). Detecting pairwise correlations in spike trains: an objective comparison of methods and application to the study of retinal waves. . J. Neurosci. *34*, pp. 14288–14303.

Daw, M.I., Tricoire, L., Erdelyi, F., Szabo, G., and McBain, C.J. (2009). Asynchronous transmitter release from cholecystokinin-containing inhibitory interneurons is widespread and target-cell independent. J. Neurosci. *29*, 11112–11122.

de la Rocha, J., Doiron, B., Shea-Brown, E., Josić, K., and Reyes, A. (2007). Correlation between neural spike trains increases with firing rate. Nature *448*, 802–806.

Deleuze, C., Bhumbra, G.S., Pazienti, A., Lourenço, J., Mailhes, C., Aguirre, A., Beato, M., and Bacci, A. (2019). Strong preference for autaptic self-connectivity

of neocortical PV interneurons facilitates their tuning to gamma-oscillations. PLoS Biol. *17*, e3000419.

Denker, M., Yegenoglu, A., Grün, S. (2018). Collaborative HPC-enabled workflows on the HBP Collaboratory using the Elephant framework. Neuroinformatics 2018, P19.

Dipoppa, M., Ranson, A., Krumin, M., Pachitariu, M., Carandini, M., and Harris, K.D. (2018). Vision and locomotion shape the interactions between neuron types in mouse visual cortex. Neuron *98*, 602–615.e8.

Dong, A., He, K., Dudok, B., Farrell, J.S., Guan, W., Liput, D.J., Puhl, H.L., Cai, R., Wang, H., Duan, J., et al. (2021). A fluorescent sensor for spatiotemporally resolved imaging of endocannabinoid dynamics in vivo. Nat. Biotechnol. *40*, 787–798.

Dudok, B., Klein, P.M., Hwaun, E., Lee, B.R., Yao, Z., Fong, O., Bowler, J.C., Terada, S., Sparks, F.T., Szabo, G.G., et al. (2021). Alternating sources of perisomatic inhibition during behavior. Neuron *109*, 997–1012.e9.

Eggan, S.M., Melchitzky, D.S., Sesack, S.R., Fish, K.N., and Lewis, D.A. (2010). Relationship of cannabinoid CB1 receptor and cholecystokinin immunoreactivity in monkey dorsolateral prefrontal cortex. Neuroscience *169*, 1651–1661.

Eggermann, E., Bucurenciu, I., Goswami, S.P., and Jonas, P. (2011). Nanodomain coupling between Ca^{2+} channels and sensors of exocytosis at fast mammalian synapses. Nat. Rev. Neurosci. *13*, 7–21.

El Boustani, S., and Destexhe, A. (2009). A master equation formalism for macroscopic modeling of asynchronous irregular activity states. Neural Comput. *21*, 46–100.

Farrell, J.S., Colangeli, R., Dong, A., George, A.G., Addo-Osafo, K., Kingsley, P.J., Morena, M., Wolff, M.D., Dudok, B., He, K., et al. (2021). In vivo endocannabinoid dynamics at the timescale of physiological and pathological neural activity. Neuron *109*, 2398–2403.e4.

Földy, C., Lee, S.Y., Szabadics, J., Neu, A., and Soltesz, I. (2007). Cell type-specific gating of perisomatic inhibition by cholecystokinin. Nat. Neurosci. *10*, 1128–1130.

Földy, C., Neu, A., Jones, M.V., and Soltesz, I. (2006). Presynaptic, activity-dependent modulation of cannabinoid type 1 receptor-mediated inhibition of GABA release. J. Neurosci. *26*, 1465–1469.

Freund, T.F., and Katona, I. (2007). Perisomatic inhibition. Neuron *56*, 33–42.

Gabernet, L., Jadhav, S.P., Feldman, D.E., Carandini, M., and Scanziani, M. (2005). Somatosensory integration controlled by dynamic thalamocortical feed-forward inhibition. Neuron *48*, 315–327.

Galarreta, M., Erdélyi, F., Szabó, G., and Hestrin, S. (2008). Cannabinoid sensitivity and synaptic properties of 2 GABAergic networks in the neocortex. Cereb. Cortex *18*, 2296–2305.

Glass, M., Dragunow, M., and Faull, R.L. (1997). Cannabinoid receptors in the human brain: a detailed anatomical and quantitative autoradiographic study in the fetal, neonatal and adult human brain. Neuroscience *77*, 299–318.

Glickfeld, L.L., and Olsen, S.R. (2017). Higher-order areas of the mouse visual cortex. Annu. Rev. Vis. Sci. *3*, 251–273.

Hájos, N., Katona, I., Naiem, S.S., Mackie, K., Ledent, C., Mody, I., and Freund, T.F. (2000). Cannabinoids inhibit hippocampal GABAergic transmission and network oscillations. Eur. J. Neurosci. *12*, 3239–3249.

Harris, K.D., and Shepherd, G.M.G. (2015). The neocortical circuit: themes and variations. Nat. Neurosci. *18*, 170–181.

Hefft, S., Kraushaar, U., Geiger, J.R.P., and Jonas, P. (2002). Presynaptic short-term depression is maintained during regulation of transmitter release at a GABAergic synapse in rat hippocampus. J. Physiol. *539*, 201–208.

Hefft, S., and Jonas, P. (2005). Asynchronous GABA release generates long-lasting inhibition at a hippocampal interneuron-principal neuron synapse. Nat. Neurosci. *8*, 1319–1328.

Heifets, B.D., Chevaleyre, V., and Castillo, P.E. (2008). Interneuron activity controls endocannabinoid-mediated presynaptic plasticity through calcineurin. Proc. Natl. Acad. Sci. USA *105*, 10250–10255.

Isaacson, J.S., and Scanziani, M. (2011). How inhibition shapes cortical activity. Neuron *72*, 231–243.

Jiang, B., Huang, S., de Pasquale, R., Millman, D., Song, L., Lee, H.K., Tsumoto, T., and Kirkwood, A. (2010). The maturation of GABAergic transmission in visual cortex requires endocannabinoid-mediated LTD of inhibitory inputs during a critical period. Neuron *66*, 248–259.

Jiang, X., Shen, S., Cadwell, C.R., Berens, P., Sinz, F., Ecker, A.S., Patel, S., and Tolias, A.S. (2015). Principles of connectivity among morphologically defined cell types in adult neocortex. Science *350*, aac9462.

Jin, M., and Glickfeld, L.L. (2020). Mouse higher visual areas provide both distributed and specialized contributions to visually guided behaviors. Curr. Biol. *30*, 4682–4692.e7.

Kano, M., Ohno-Shosaku, T., Hashimotodani, Y., Uchigashima, M., and Watanabe, M. (2009). Endocannabinoid-mediated control of synaptic transmission. Physiol. Rev. *89*, 309–380.

Katona, I., Sperlágh, B., Sík, A., Käfalvi, A., Vizi, E.S., Mackie, K., and Freund, T.F. (1999). Presynaptically located CB1 cannabinoid receptors regulate GABA release from axon terminals of specific hippocampal interneurons. J. Neurosci. *19*, 4544–4558.

Katona, I., Urban, G.M., Wallace, M., Ledent, C., Jung, K.M., Piomelli, D., Mackie, K., and Freund, T.F. (2006). Molecular composition of the endocannabinoid system at glutamatergic synapses. J. Neurosci. *26*, 5628–5637.

Keller, A.J., Roth, M.M., and Scanziani, M. (2020). Feedback generates a second receptive field in neurons of the visual cortex. Nature *582*, 545–549.

Kepecs, A., and Fishell, G. (2014). Interneuron cell types are fit to function. Nature *505*, 318–326.

Kim, J., and Alger, B.E. (2001). Random response fluctuations lead to spurious paired-pulse facilitation. J. Neurosci. *21*, 9608–9618.

Koukouli, F., Rooy, M., Tziotis, D., Sailor, K.A., O'Neill, H.C., Levenga, J., Witte, M., Nilges, M., Changeux, J.P., Hoeffer, C.A., et al. (2017). Nicotine reverses hypofrontality in animal models of addiction and schizophrenia. Nat. Med. *23*, 347–354.

Kumar, A., Rotter, S., and Aertsen, A. (2008). Conditions for propagating synchronous spiking and asynchronous firing rates in a cortical network model. J. Neurosci. *28*, 5268–5280.

Ladarre, D., Roland, A.B., Biedzinski, S., Ricobaraza, A., and Lenkei, Z. (2014). Polarized cellular patterns of endocannabinoid production and detection shape cannabinoid signaling in neurons. Front. Cell. Neurosci. *8*, 426.

Larkum, M. (2013). A cellular mechanism for cortical associations: an organizing principle for the cerebral cortex. Trends Neurosci. *36*, 141–151.

Lee, S.H., Földy, C., and Soltesz, I. (2010). Distinct endocannabinoid control of GABA release at perisomatic and dendritic synapses in the hippocampus. J. Neurosci. *30*, 7993–8000.

Lee, S.H., Kwan, A.C., Zhang, S., Phoumthipphavong, V., Flannery, J.G., Masmanidis, S.C., Taniguchi, H., Huang, Z.J., Zhang, F., Boyden, E.S., et al. (2012). Activation of specific interneurons improves V1 feature selectivity and visual perception. Nature *488*, 379–383.

Lee, S.H., Ledri, M., Tóth, B., Marchionni, I., Henstridge, C.M., Dudok, B., Kenesei, K., Barna, L., Szabó, S.I., Renkecz, T., et al. (2015). Multiple forms of endocannabinoid and endovanilloid signaling regulate the tonic control of GABA release. J. Neurosci. *35*, 10039–10057.

Leterrier, C., Bonnard, D., Carrel, D., Rossier, J., and Lenkei, Z. (2004). Constitutive endocytic cycle of the CB1 cannabinoid receptor. J. Biol. Chem. *279*, 36013–36021.

Losonczy, A., Biró, A.A., and Nusser, Z. (2004). Persistently active cannabinoid receptors mute a subpopulation of hippocampal interneurons. Proc. Natl. Acad. Sci. USA *101*, 1362–1367.

Lourenço, J., Cannich, A., Carta, M., Coussen, F., Mulle, C., and Marsicano, G. (2010). Synaptic activation of kainate receptors gates presynaptic CB(1) signaling at GABAergic synapses. Nat. Neurosci. *13*, 197–204.

Lourenço, J., De Stasi, A.M., Deleuze, C., Bigot, M., Pazienti, A., Aguirre, A., Giugliano, M., Ostojic, S., and Bacci, A. (2020a). Modulation of coordinated

activity across cortical layers by plasticity of inhibitory synapses. Cell Rep. *30*, 630–641.e5.

Lourenço, J., Koukouli, F., and Bacci, A. (2020b). Synaptic inhibition in the neocortex: orchestration and computation through canonical circuits and variations on the theme. Cortex *132*, 258–280.

Lourenço, J., Pacioni, S., Rebola, N., van Woerden, G.M., Marinelli, S., DiGregorio, D., and Bacci, A. (2014). Non-associative potentiation of perisomatic inhibition alters the temporal coding of neocortical layer 5 pyramidal neurons. PLoS Biol. *12*, e1001903.

Maejima, T., Hashimoto, K., Yoshida, T., Aiba, A., and Kano, M. (2001). Presynaptic inhibition caused by retrograde signal from metabotropic glutamate to cannabinoid receptors. Neuron *31*, 463–475.

Manseau, F., Marinelli, S., Méndez, P., Schwaller, B., Prince, D.A., Huguenard, J.R., and Bacci, A. (2010). Desynchronization of neocortical networks by asynchronous release of GABA at autaptic and synaptic contacts from fast-spiking interneurons. PLoS Biol. *8*, e1000492.

Marinelli, S., Pacioni, S., Cannich, A., Marsicano, G., and Bacci, A. (2009). Self-modulation of neocortical pyramidal neurons by endocannabinoids. Nat. Neurosci. *12*, 1488–1490.

Markram, H., Toledo-Rodriguez, M., Wang, Y., Gupta, A., Silberberg, G., and Wu, C. (2004). Interneurons of the neocortical inhibitory system. Nat. Rev. Neurosci. *5*, 793–807.

Marsicano, G., and Lutz, B. (1999). Expression of the cannabinoid receptor CB1 in distinct neuronal subpopulations in the adult mouse forebrain. Eur. J. Neurosci. *11*, 4213–4225.

Marsicano, G., Wotjak, C.T., Azad, S.C., Bisogno, T., Rammes, G., Cascio, M.G., Hermann, H., Tang, J., Hofmann, C., Zieglgänsberger, W., et al. (2002). The endogenous cannabinoid system controls extinction of aversive memories. Nature *418*, 530–534.

McGinley, M.J., Vinck, M., Reimer, J., Batista-Brito, R., Zagha, E., Cadwell, C.R., Tolias, A.S., Cardin, J.A., and McCormick, D.A. (2015). Waking state: rapid variations modulate neural and behavioral responses. Neuron *87*, 1143–1161.

Minderer, M., Brown, K.D., and Harvey, C.D. (2019). The spatial structure of neural encoding in mouse posterior cortex during navigation. Neuron *102*, 232–248.e11.

Murgas, K.A., Wilson, A.M., Michael, V., and Glickfeld, L.L. (2020). Unique spatial integration in mouse primary visual cortex and higher visual areas. J. Neurosci. *40*, 1862–1873.

Naka, A., Veit, J., Shababo, B., Chance, R.K., Risso, D., Stafford, D., Snyder, B., Egladyous, A., Chu, D., Sridharan, S., et al. (2019). Complementary networks of cortical somatostatin interneurons enforce layer specific control. Elife *8*, e43696.

Neu, A., Földy, C., and Soltesz, I. (2007). Postsynaptic origin of CB1-dependent tonic inhibition of GABA release at cholecystokinin-positive basket cell to pyramidal cell synapses in the CA1 region of the rat hippocampus. J. Physiol. *578*, 233–247.

Nestvogel, D.B., and McCormick, D.A. (2022). Visual thalamocortical mechanisms of waking state-dependent activity and alpha oscillations. Neuron *110*, 120–138.e4.

Niell, C.M., and Stryker, M.P. (2010). Modulation of visual responses by behavioral state in mouse visual cortex. Neuron *65*, 472–479.

Oliveira da Cruz, J.F., Busquets-Garcia, A., Zhao, Z., Varilh, M., Lavanco, G., Bellocchio, L., Robin, L., Cannich, A., Julio-Kalajzić, F., Lesté-Lasserre, T., et al. (2020). Specific hippocampal interneurons shape consolidation of recognition memory. Cell Rep. *32*, 108046.

Paul, A., Crow, M., Raudales, R., He, M., Gillis, J., and Huang, Z.J. (2017). Transcriptional architecture of synaptic communication delineates GABAergic neuron identity. Cell *171*, 522–539.e20.

Petersen, C.C.H., and Crochet, S. (2013). Synaptic computation and sensory processing in neocortical layer 2/3. Neuron *78*, 28–48.

Pfeffer, C.K., Xue, M., He, M., Huang, Z.J., and Scanziani, M. (2013). Inhibition of inhibition in visual cortex: the logic of connections between molecularly distinct interneurons. Nat. Neurosci. *16*, 1068–1076.

Pouille, F., and Scanziani, M. (2001). Enforcement of temporal fidelity in pyramidal cells by somatic feed-forward inhibition. Science *293*, 1159–1163.

Poulet, J.F.A., Fernandez, L.M.J., Crochet, S., and Petersen, C.C.H. (2012). Thalamic control of cortical states. Nat. Neurosci. *15*, 370–372.

Renart, A., de la Rocha, J., Bartho, P., Hollender, L., Parga, N., Reyes, A., and Harris, K.D. (2010). The asynchronous state in cortical circuits. Science *327*, 587–590.

Rinaldi-Carmona, M., Barth, F., Héaulme, M., Shire, D., Calandra, B., Congy, C., Martinez, S., Maruani, J., Néliat, G., Caput, D., et al. (1994). SR141716A, a potent and selective antagonist of the brain cannabinoid receptor. FEBS Lett. *350*, 240–244.

Romano, S.A., Pérez-Schuster, V., Jouary, A., Boulanger-Weill, J., Candeo, A., Pietri, T., and Sumbre, G. (2017). An integrated calcium imaging processing toolbox for the analysis of neuronal population dynamics. PLoS Comput. Biol. *13*, e1005526.

Robbe, D., Montgomery, S.M., Thome, A., Rueda-Orozco, P.E., McNaughton, B.L., and Buzsaki, G. (2006). Cannabinoids reveal importance of spike timing coordination in hippocampal function. Nat. Neurosci. *9*, 1526–1533.

Rovira-Esteban, L., Péterfi, Z., Vikór, A., Máté, Z., Szabó, G., and Hájos, N. (2017). Morphological and physiological properties of CCK/CB1R-expressing interneurons in the basal amygdala. Brain Struct. Funct. *222*, 3543–3565.

Saleem, A.B. (2020). Two stream hypothesis of visual processing for navigation in mouse. Curr. Opin. Neurobiol. *64*, 70–78.

Saleem, A.B., Ayaz, A., Jeffery, K.J., Harris, K.D., and Carandini, M. (2013). Integration of visual motion and locomotion in mouse visual cortex. Nat. Neurosci. *16*, 1864–1869.

Saravia, R., Flores, Á., Plaza-Zabala, A., Busquets-Garcia, A., Pastor, A., de la Torre, R., Di Marzo, V., Marsicano, G., Ozaita, A., Maldonado, R., and Berrendero, F. (2017). CB(1) cannabinoid receptors mediate cognitive deficits and structural plasticity changes during nicotine withdrawal. Biol. Psychiatry *81*, 625–634.

Siegle, J.H., Pritchett, D.L., and Moore, C.I. (2014). Gamma-range synchronization of fast-spiking interneurons can enhance detection of tactile stimuli. Nat. Neurosci. *17*, 1371–1379.

Siegle, J.H., Jia, X., Durand, S., Gale, S., Bennett, C., Graddis, N., Heller, G., Ramirez, T.K., Choi, H., Luviano, J.A., et al. (2021). Survey of spiking in the mouse visual system reveals functional hierarchy. Nature *592*, 86–92.

Stimberg, M., Brette, R., and Goodman, D.F. (2019). Brian 2, an intuitive and efficient neural simulator. Elife *8*, e47314.

Soria-Gomez, E., Bellocchio, L., Reguero, L., Lepousez, G., Martin, C., Bendahmane, M., Ruehle, S., Remmers, F., Desprez, T., Matias, I., et al. (2014). The endocannabinoid system controls food intake via olfactory processes. Nat. Neurosci. *17*, 407–415.

Soria-Gómez, E., Busquets-Garcia, A., Hu, F., Mehidi, A., Cannich, A., Roux, L., Louit, I., Alonso, L., Wiesner, T., Georges, F., et al. (2015). Habenular CB1 receptors control the expression of aversive memories. Neuron *88*, 306–313.

Stringer, C., and Pachitariu, M. (2019). Computational processing of neural recordings from calcium imaging data. Curr. Opin. Neurobiol. *55*, 22–31.

Stringer, C., Pachitariu, M., Steinmetz, N., Reddy, C.B., Carandini, M., and Harris, K.D. (2019). Spontaneous behaviors drive multidimensional, brainwide activity. Science *364*, 255.

Tremblay, R., Lee, S., and Rudy, B. (2016). GABAergic interneurons in the neocortex: from cellular properties to circuits. Neuron *91*, 260–292.

Varvel, S.A., Anum, E.A., and Lichtman, A.H. (2005). Disruption of CB(1) receptor signaling impairs extinction of spatial memory in mice. Psychopharmacology (Berl) *179*, 863–872.

Vogels, T.P., and Abbott, L.F. (2005). Signal propagation and logic gating in networks of integrate-and-fire neurons. J. Neurosci. *25*, 10786–10795.

Wamsteeker Cusulin, J.I., Senst, L., Teskey, G.C., and Bains, J.S. (2014). Experience salience gates endocannabinoid signaling at hypothalamic synapses. J. Neurosci. *34*, 6177–6181.

Wilson, N.R., Runyan, C.A., Wang, F.L., and Sur, M. (2012). Division and subtraction by distinct cortical inhibitory networks in vivo. Nature *488*, 343–348.

Wilson, R.I., Kunos, G., and Nicoll, R.A. (2001). Presynaptic specificity of endocannabinoid signaling in the hippocampus. Neuron *31*, 453–462.

Wilson, R.I., and Nicoll, R.A. (2001). Endogenous cannabinoids mediate retrograde signalling at hippocampal synapses. Nature *410*, 588–592.

Winters, B.D., Krüger, J.M., Huang, X., Gallaher, Z.R., Ishikawa, M., Czaja, K., Krueger, J.M., Huang, Y.H., Schlüter, O.M., and Dong, Y. (2012). Cannabinoid receptor 1-expressing neurons in the nucleus accumbens. Proc. Natl. Acad. Sci. USA *109*, E2717–E2725.

Yoneda, T., Kameyama, K., Esumi, K., Daimyo, Y., Watanabe, M., and Hata, Y. (2013). Developmental and visual input-dependent regulation of the CB1 cannabinoid receptor in the mouse visual cortex. PLoS One *8*, e53082.

Younts, T.J., and Castillo, P.E. (2014). Endogenous cannabinoid signaling at inhibitory interneurons. Curr. Opin. Neurobiol. *26*, 42–50.

Zerlaut, Y., Zucca, S., Panzeri, S., and Fellin, T. (2019). The spectrum of asynchronous dynamics in spiking networks as a model for the diversity of non-rhythmic waking states in the neocortex. Cell Rep. *27*, 1119–1132.e7.

Zhu, P.J., and Lovinger, D.M. (2007). Persistent synaptic activity produces long-lasting enhancement of endocannabinoid modulation and alters long-term synaptic plasticity. J. Neurophysiol. *97*, 4386–4389.

STAR★METHODS

KEY RESOURCES TABLE

REAGENT or RESOURCE	SOURCE	IDENTIFIER
Antibodies		
Anti-CB1 (goat)	Frontiers Institute	CB1-Go-Af450; RRID: AB_2571530
Anti-GFP (mouse)	Millipore	MAB3580; RRID: AB_94936
Anti-DsRed (rabbit)	Clontech/Takara Bio	632496; RRID: AB_10013483
Anti-PV (mouse)	Sigma-Aldrich	P3088; RRID: AB_477329
Anti-SST (mouse)	Santa Cruz	G10 sc-55565; RRID: AB_831726
Alexa 488 anti-mouse	Life Technologies	A11029; RRID: AB_2534088
Alexa 488 anti-goat	Life Technologies	A11055; RRID: AB_2534102
Alexa 633 anti-rabbit	Life Technologies	A21071; RRID: AB_2535732
Anti-DIG	Roche	11207733910; RRID: AB_514500
NeutrAvidin Dylight 633	Invitrogen	22844; RRID: AB_11154451
Anti-rabbit IgG, HRP-linked	Cell Signaling Technology	7074; RRID: AB_2099233
Bacterial and virus strains		
AAV.syn.GCaMP6f.WPRE.SV40	Addgene	100837-AAV1
AAV.CAG.tdTomato.WPRE.SV40	Addgene	105554-AAV1
AAV-CAG-Cre	Giovanni Marsicano	Soria-Gomez et al. (2014)
AAV9-hsyn-eCB2	WZ Biosciences	YL009008-AV9
Chemicals, peptides, and recombinant proteins		
Biocytin	Sigma-Aldrich	B42611
K-gluconate	Sigma-Aldrich	G4500
KCl	Sigma-Aldrich	P4504
HEPES	Sigma-Aldrich	H4034
EGTA	Sigma-Aldrich	E4378
$MgCl_2$	Sigma-Aldrich	63069
Mg-ATP	Sigma-Aldrich	A9187
Na-GTP	Sigma-Aldrich	G8877
KOH	Sigma-Aldrich	P5958
Phosphocreatine di (tris)	Sigma-Aldrich	P1937
NaCl	Sigma-Aldrich	S7653
$NaH_2PO_4.H2O$	Sigma-Aldrich	S9638
$NaHCO_3$	Sigma-Aldrich	S6014
Choline chloride	Sigma-Aldrich	C7017
$MgSO_4$	Sigma-Aldrich	M2643
$CaCl_2.2H_20$	Sigma-Aldrich	C7902
D-(+)-Glucose	Sigma-Aldrich	G6152
Tween80	Sigma-Aldrich	P1754
Triton X-100	Sigma-Aldrich	T8787
DMSO	Sigma-Aldrich	D2650
D-AP5	Tocris Biosciences	0106
DNQX disodium salt	Tocris Biosciences	2312
AM 251	Tocris Biosciences	1117
SR 95531 hydrobromide	Tocris Biosciences	1262
SR 141716A (Rimonabant)	Tocris Biosciences	0923
Buprenorphine (Buprecare)	Centravet	BUP001
Paraformaldeyde Euromedex	Sigma-Aldrich	15714

(*Continued on next page*)

Continued

REAGENT or RESOURCE	SOURCE	IDENTIFIER
NEN blocking buffer	PerkinElmer	FP1012
(FITC)-labeled tyramide	PerkinElmer	NEL701001KT
Streptavidin-Texas Red	PerkinElmer	NEL721001EA
DAPI	Fisher Scientific	D1306
Ketamine, Imalgene 1000	ICM Animal House Pharmacy/Centravet	IMA004
Xylazine, Rompun	ICM Animal House Pharmacy/Centravet	ROM001
Lidocaine	ICM Animal House Pharmacy/Centravet	LAO001
Betadine	ICM Animal House Pharmacy/Centravet	PH4
Isoflurane	ICM Animal House Pharmacy/Centravet	VET066
Critical commercial assays		
DAB Substrate Kit	Abcam	ab64238
ABC (Avidin-Biotin Complex) Kit	VECTASTAIN Elite	PK-6100
TSA Plus Biotin Kit	PerkinElmer	NEL749A001KT
Dental cement, Super Bond Coffret Complet	PHYMEP	7100
Deposited data		
Spiking network model	This paper	https://doi.org/10.5281/zenodo.6795090
Experimental models: Organisms/strains		
CB1-tdTomato mouse	Oliver M. Schlüter	Winters et al. (2012)
CB1$^{floxed/floxed}$ mouse	Giovanni Marsicano	Soria-Gomez et al. (2014)
5-HT3-Cre::RCE mouse	Nathaniel Heintz	https://www.mmrrc.org/catalog/sds.php?mmrrc_id=36680
GAD67 GFP mouse	Kindly donated by Marie-Stephane Aigrot, ICM Paris	https://cir.nii.ac.jp/crid/1574231874900110464
Software and algorithms		
ImageJ	NIH	https://imagej-nih-gov.insb.bib.cnrs.fr/ij/
Prism	Prism-GraphPad	https://www.graphpad.com/scientific-software/prism/
OriginPro 2016	OriginLab	https://www.originlab.com/2016
MATLAB	Mathworks	https://www.mathworks.com/
Python	2.7.0	https://www.python.org/
pClamp 10.3	Molecular Devices	https://www.moleculardevices.com/products/axon-patch-clamp-system/acquisition-and-analysis-software/pclamp-software-suite
Other		
Head post for head-fixed animals	Luigs & Neumann	200–200 500 2133-21-59

RESOURCE AVAILABILITY

Lead contact

Further information and requests for resources and reagent should be direct to and will be fulfilled by the Lead Contact, Joana Lourenço (joana.lourenco@icm-institute.org).

Materials availability

This study did not generate new unique reagents.

Data and code availability

All data reported in this paper will be shared by the lead contact upon request.

The code for the simulating and analyzing the spiking network model is publicly available at: https://github.com/yzerlaut/CB1_ntwk_modeling and archived at: https://doi.org/10.5281/zenodo.6795090.

Any additional information required to reanalyze the data reported in this paper is available from the lead contact upon request.

EXPERIMENTAL MODEL AND SUBJECT DETAILS

Animals

Experimental procedures followed French and European guidelines for animal experimentation and in compliance with the institutional animal welfare guidelines of the Paris Brain Institute. Experiments for paired recordings were performed on both sexes aged between P30 and P40 CB1-tdTomato mice (Winters et al., 2012), except for experiments illustrated in Figure S6, for which mice were older than P60. In some experiments, CB1-tdTomato mice were crossed with GAD67-GFP mice to identify CB1-expressing INs for cell counting. In experiments for Figures 1 and S6, C57BL/6J wild-type were purchased from Janvier laboratories. Mice were housed in an animal facility with a 12h light/dark cycle, with food and water available *ad libitum*. Viral injections and chronic cranial windows for 2P Ca^{2+} imaging experiments *in vivo* were performed on two months old male mice of CB1-tdTomato or $CB1^{floxed/floxed}$ mice. Imaging sessions started following habituation, four to five weeks post-surgery for CB1-tdTomato or $CB1^{floxed/floxed}$ mice, respectively.

METHOD DETAILS

Immunohistochemistry and cell counting

All animals were deeply anesthetized with ketamine-xylazine and transcardially perfused first with cold PBS (20mL) followed by 30–40 mL of cold 4% PFA (paraformaldehyde, diluted in PBS), and brains were post-fixed in 4% PFA overnight at 4°C. For cryoprotection they were next put in 30% sucrose (diluted in PBS) overnight and frozen at - 45°C in isopentane. The brains were cut with a freezing microtome (Thermo Fisher), with nominal section thickness set to 20 μm. After rinsing with PBS, slices where incubated 2h at room temperature in 0.3% PBT (0.3% Triton X- in PBS) and 10% BSA blocking solution. Primary antibodies diluted in 0.3% PBT and 0.1% NGS (normal goat serum) were incubated overnight at 4°C. The following antibodies were used: anti-CB1 (Frontiers institute, goat 1:400), anti-GFP (Millipore, MAB 3580 mouse 1:500), anti-DsRed (Clontech, rabbit 1:500), anti-PV (Sigma PARV-19, mouse 1:1000) and anti-SST (Santa Cruz G10 sc-55565, mouse 1:250). Slices were then rinsed with PBS and incubated for 2h at room temperature with the secondary antibodies Alexa 488 anti-goat, Alexa 488 anti-mouse and Alexa 633 anti-rabbit, all obtained from Life Technologies and diluted 1:500 in PBT 0.3%. Slices were mounted with DAPI Fluoromount (Sigma) and stocked at 4°C. Whole brain slices were imaged using an epifluorescence slice scanner (Axio scan Z1 Zeiss, magnification 20×).

CB1 immunofluorescence pattern

Only slices in which both V1 and V2M areas were present were analyzed in order to be able to quantitatively compare the fluorescence patterns. To obtain the pattern, the "straight" option in FIJI (NIH) with a line width of 390 μm was used to calculate the gray value intensity of CB1 immuno-staining from pia to white matter. For each slice, the maximum fluorescence intensity over a length of 10 μm of either V1 and V2 was used to normalize fluorescence in the rest of the analyzed areas. Moreover, due to differences in cortical length between animals and slices, we determined cortical layer thickness by using a ratio obtained from measuring each layer in the Allen atlas with total cortical length set as 1.

Combined fluorescent *in situ* hybridization (FISH)/Immunohistochemistry (IHC) on free-floating frozen sections

CB1 FISH/tdTomato immunofluorescence experiments were carried out as previously described (Marsicano and Lutz, 1999; Oliveira da Cruz et al., 2020). Briefly, free-floating frozen coronal sections were cut out with a cryostat (20 μm, cryostat Leica CM1950), collected in an antifreeze solution and conserved at −20°C. After inactivation of endogenous peroxidases and blocking with Avidin/Biotin Blocking Kit (Vector Labs, USA), sections were incubated overnight at 4°C with antiDsRed rabbit polyclonal primary antibody (1:1000, 632496 Takara Bio) diluted in a Triton buffer. The following day, the sections were incubated with a secondary antibody goat anti-rabbit conjugated to a horseradish peroxidase (HRP) (1:500, 7074S Cell Signaling Technology) followed by an incubation at RT with TSA plus Biotin System (Biotin TSA 1:250, NEL749A001KT PerkinElmer). Sections were hybridized overnight at 70°C with Digoxigenin (DIG)-labeled riboprobe against mouse CB1 receptor (1:1000, prepared as described in Marsicano and Lutz, 1999). CB1 receptor hybridization was revealed by a TSA reaction using cyanine 3 (Cy3)-labeled tyramide (1:100 for 10 min, NEL744001KT PerkinElmer). CCK FISH/tdTomato immunofluorescence experiments were carried out as described just above and as previously reported (Oliveira da Cruz et al., 2020). In this case, the sections were hybridized overnight at 60°C with Digoxigenin (DIG)-labeled riboprobe against CCK (1:1000, (Marsicano and Lutz, 1999), and the signal of CCK hybridization was revealed by a TSA reaction using fluorescein isothiocyanate (FITC)-labeled tyramide (1:100 for 10 min, NEL741001KT PerkinElmer). Finally, the slices were incubated with DAPI (1:20000; 11530306 Fisher Scientific) diluted in PBS, following by several washes, to finally be mounted, cover slipped and imaged using an epifluorescence slice scanner (Axio scan Z1 Zeiss, magnification 20×) (see below section on "Counting CB1 INs" for analysis).

Counting CB1 INs

CB1-tdTomato/GAD67-GFP positive cells were counted in both V1 and V2; for each area a region of interest (ROI) was drawn. The ITCN (Image-based Tool for Counting Nuclei) plugin in ImageJ was modified (courtesy of Brahim Abbes, Neurostack) in order to be able to count the cells and their distance from the pia simultaneously. The pia was traced on each image, and cells expressing both

tdTomato and GFP were manually marked. The software then calculated the minimal distance from marked cells to the pia. Once these distances were established, we were able to bin cell counts in the different layers of the cortex. Layer (bin) size was determined using the Allen brain atlas, determining the % of cortical thickness each layer represented. We then used these ratios to calculate actual layer thickness on our slices. Also, ROIs could differ widely in width, hence to compensate for this we divided the obtained laminar density by the width of the ROI.

In vitro slice preparation for electrophysiological recordings

Coronal slices (350 μm thick) of visual cortex were obtained from mice of both sexes aged between P30 and P40. The area of interest was identified using the Allen adult mouse brain reference atlas. Animals were deeply anesthetized with a mix containing 120 mg/kg ketamine and 24 Xylazine mg/kg of body weight (in 0.9% NaCl). A transcardiac perfusion was performed using an ice-cold "cutting" solution containing the following (in mM): 126 choline chloride, 16 glucose, 26 $NaHCO_2$, 2.5 KCl, 1.25 NaH2PO_4, 7 $MgSO_4$, 0.5 $CaCl_2$, (equilibrated with 95% O_2/5% CO_2). Following decapitation, brains were quickly removed and sliced with a vibratome (Leica) while immersed in ice-cold cutting solution. Slices were then incubated in oxygenated (95% O_2/5% CO_2) artificial cerebrospinal fluid (ASCF) containing the following (in mM): 126 NaCl, 20 glucose, 26 $NaHCO_3$, 2.5 KCl, 1.25 NaH_2PO_4, 1 $MgSO_4$, 2$CaCl_2$ (pH 7.4, 310–320mOsm/L), at 34°C for 20 min, and subsequently at room temperature before transferring to the recording chamber. The recording chamber was constantly perfused with warm (32 ± 1°C), oxygenated ACSF at 2.5–3 mL/min.

Electrophysiology

Synaptic currents were recorded in whole-cell voltage or current clamp mode in principal cells of either L2/3 or L4 of primary and secondary visual cortex. Excitatory cells of L2/3 were visually identified by their triangular soma and apical dendrites projecting toward the pia, while in L4 they were identified by their round soma and by verifying their regular firing properties. Meanwhile, CB1 BCs were targeted using CB1-tdTomato fluorescence elicited by a green (λ = 530 nm) LED (Cairn research) coupled to the epifluorescence path of the microscope, alongside their characteristic large soma and bior multipolar dendritic morphology. To identify V1 and V2M, we guided ourselves using the Allen brain atlas. We refer to V2M including both antero-medial (AM) and postero-medial (PM) visual areas as defined in the Allen brain atlas. To study the passive properties of CB1 BCs, action potential waveform and firing dynamics, electrodes were filled with an intracellular solution containing (in mM): 135 K-gluconate, 5 KCl,10 HEPES, 0.01 EGTA, 4 Mg-ATP, 0.3 Na-GTP and 10 phosphocreatine di(tris). For recording in slices from older animals (Figure S6), 10 mM of GABA were added to the intracellular solution. The pH adjusted with KOH to 7.2 resulting in an osmolarity of 290–300 mOsm. Based on the Nernst equation, the estimated reversal potential for chloride (ECl) was approximately −84 mV. For these experiments, the following drugs were also present in the superfusate (in μM): 10 DNQX, 10 gabazine, and 50 D-APV (all from Tocris).

To record GABAergic uIPSCs from paired recordings, we used a "high chloride" intracellular solution containing (in mM): 70 K-gluconate, 70 KCl, 10 HEPES, 0.2 EGTA, 2 $MgCl_2$, 0.5 $CaCl_2$, 4 Mg-ATP, 0.3 Na-GTP, 5 phosphocreatine di(tris); again, the pH was adjusted to 7.2 with KOH and resulted in an osmolarity of 290–300 mOsm. For this solution, the ECl was calculated to be at ∼ -13 mV based on the Nernst equation, which means that when clamping the cell at −70mV, activation of GABAA receptors resulted in inward currents. We confirmed that the currents were GABAergic by demonstrating they were unaffected by DNQX (10 μM) (Tocris Bioscience) and blocked by gabazine (10 μM; *data not shown*). In most paired-recording experiments, the ACSF was left drug-free as CB1 BCs were reliably targeted. The distance between the presynaptic and postsynaptic neuron was consistently less than ∼50 μm in both cortical areas for recordings within L2/3, and less than ∼100 μm for L2/3 → L4 recordings. We interleaved V1 and V2M recordings throughout the entire duration of each experiment and in each condition, to prevent a possible bias originating from slice deterioration with time. Signals were amplified using a Multiclamp 700B patch-clamp amplifier (Axon Instruments), digitized with a Digidata 1440A (Axon Instruments), sampled at 50 kHz and filtered at 2 kHz or 10 kHz, respectively for voltage and current clamp recordings.

pClamp v. 10.3 (Axon instruments) was used to record the signal and generate stimulation protocols. All voltage-clamp protocols contained a 5 mV step used to monitor the series resistance (Rs), which was kept under 15 MΩ for postsynaptic neurons and under 25 MΩ for presynaptic neurons (as this did not prevent evoking unclamped action currents). Recordings in which the Rs had deviated by more than 20% were discarded. For paired recordings, a brief pulse was used to elicit a single action current, followed by a train of 5 pulses at 50 Hz. This pattern was repeated every 5s (0.2 Hz). In Figure 2, in order to test for presynaptic modulation, four trains of action potentials (10 pulses at 50 Hz, inter-train interval of 300ms) were elicited in the presynaptic CB1 BC.

Single action potential waveform, firing dynamics and synaptic properties (uIPSC amplitudes, failure rate, charge, PPR) were obtained using custom scripts in MATLAB. Synaptic failures were defined as any value inferior to twice the standard deviation of the noise.

AM251 pharmacology: The CB1 antagonist AM251 (3 μM) was not applied acutely, but uIPSCs were tested in separate groups pre-incubated with either vehicle or AM-251. This was necessary, as AM-251 take several tens of minutes of perfusion to block CB1Rs.

Morphological reconstruction

Biocytin Fills: Biocytin (Sigma) was added to the intracellular solution at a high concentration (0.5g/100mL) (Jiang et al., 2015)and neurons were kept in whole-cell configuration mode for an hour during which large depolarizing currents in current clamp mode were applied for fifteen times (100ms, 1-2nA, 1Hz). At the end of recordings, the patch pipette was removed carefully with the

aim of resealing the cell properly, equivalent to obtaining an outside-out patch. The slice was then left in the recording chamber for a further 5–10 min to allow further diffusion. Slices were then fixed with 4% paraformaldehyde in phosphate buffer saline (PBS, Sigma) for at least 48 h. Following fixation, slices were incubated with the avidin-biotin complex (Vector Labs) and a high concentration of detergent (Triton X-100, 5%) for at least two days before staining with 3,3′Diaminobenzidine (DAB, AbCam).

Cells were then reconstructed and cortical layers delimited using neurolucida 7 (MBF Bioscience) and the most up to date mouse atlas (Allen Institute). Because cortical layer thickness differs within and across areas, we normalized neurite lengths relative to layer thickness to obtain the most accurate measure of density in each layer using an arithmetic method (Bortone et al., 2014). To obtain heat maps, we imported reconstructions in Illustrator (Adobe) and aligned the soma horizontally, and pia and white matter vertically. From there, individual bitmaps were generated separating dendrites and axons. These were subsequently blurred in ImageJ (NIH) using a Gaussian filter with a radius equivalent to 20 μm. The contrast of blurred images was then adjusted to obtain the highest possible pixel intensity, and were then overlapped and averaged. The resulting group average image was also adjusted to the highest pixel intensity, and a lookup table (ImageJ's "Fire", inverted) was applied to color code the density of neurites across cortical layers.

Two-photon imaging of eCB in acute mouse brain slices

C57BL/6J pups (P1) were anesthetized on ice, and a beveled injection pipette, attached to a micromanipulator, was gently inserted 300 μm deep in the visual cortex through intact skin and skull. We then delivered 400 nL of viral particles AAV2/9.hSyn.GRAB-eCB2.0 (WZ Biosciences) using an injector (Nanoliter, 2000 Injector, WPI Inc., USA), and the pipette was left in place for an additional 30 s, before it was retracted. For 2P eCB imaging experiments, coronal slices (350 μm thick) of visual cortex were obtained from mice of both sexes aged between P45-61, as described above. Two-photon imaging was performed using an Olympus B61WIF microscope (Olympus, France) equipped with a ×20, 0.5-NA water-immersion objective (Olympus, France) and a femtosecond pulsed Ti:Sapphire laser (Chameleon Vision II, Coherent) tuned to 920-nm. Fluorescence light was separated from the excitation path through a long pass dichroic (660dcxr; Chroma, USA), split into green and red channels with a second long pass dichroic (575dcxr; Chroma, USA), and cleaned up with band pass filters (hq525/70 and hq607/45; Chroma, USA). Fluorescence was detected using both proximal epifluorescence and substage gallium arsenide phosphide photomultiplier tubes (H10770PA-40, Hamamatsu). Time-lapse imaging to monitor variations in eCB2.0 fluorescence was performed over periods of 30 min in either V1 or V2M at the frame rate of 0.17 Hz (512 × 512; 1.151X1.151 μm/pixel, dwell time 1.2 μsec). In experiments of Figure S5, eCB2.0 fluorescence signals were corrected for photobleaching by fitting a biexponential curve to the baseline period and subtracted from the raw fluorescence. After correction for photobleaching fluorescence traces were then converted to final $\Delta F/F(t)$.

Virus injections and chronic cranial window preparation

Virus injections and implantation of the cranial windows were performed as previously described (Koukouli et al., 2017). Mice were anesthetized using a mixture of ketamine (Imalgen 1000; Rhone Mérieux) and xylazine (Rompun; Bayer AG), 10 mL/kg i.p. and placed into a stereotaxic frame. The body temperature was maintained at ~37°C using a regulated heating blanket and a thermal probe. Eye ointment was applied to prevent dehydration. Before skin incision, mice were treated with buprenorphine (0.1 mg/kg i.p.) and lidocaine (0.4 mL/kg of a 1% solution, local application). After hair removal and disinfection with betadine and ethanol, the skin was opened, and the exposed cranial bone was cleaned and dried with cotton pads. For calcium imaging of cortical neurons we used separate groups of mice in which we infected either V1 or V2M with the genetically encoded indicator GCaMP6f following the coordinates of the Paxinos mouse brain atlas. We injected 200 nL of AAV1.syn.GCaMP6f.WPRE.SV40 (1×10^{13} vg/mL, University of Pennsylvania Vector Core) at the following coordinates, V1:AP, −2.54 mm from bregma, L, +2.5; DV, −0.3 to - 0.1 mm and V2M: AP, −2.54 mm from bregma, L, +1.25; DV, −0.3 to - 0.1 mm from the skull using a Nanoject II™ (Drummond Scientific) at a slow infusion rate (23 nL/s). For local deletion of CB1 receptors in layers 2/3 of V1 or V2M, $CB1^{floxed/floxed}$ mice were injected with an AAV-CAG-Cre (0.5 μL) (Soria-Gomez et al., 2014) or a control virus AAV1.CAG.tdTomato.WPRE.SV40 (1.52×10^{13} GC/mL, University of Pennsylvania Vector Core). Animals were used for experiments five weeks after injection (Figures 5 and S8) in order to have an optimal deletion of CB1, as previously described (Soria-Gomez et al., 2014, 2015). After injection, the pipette was left *in situ* for an additional 5 min to prevent backflow. A circular cover glass (5 mm diameter) was placed over the exposed region and the glass edge was sealed to the skull with dental cement (Coffret SUPERBOND complete, Phymep). A circle stainless steel head post (Luigs & Neumann) was fixed to the mouse skull using dental cement.

Habituation of the mice for awake imaging

Three weeks after the cranial surgery, mice were first habituated to the experimenter by handling. Mice were then accustomed to the imaging environment, where they freely moved on a rotating disk while being head-fixed. All two-photon Ca^{2+} imaging experiments were performed in the dark without any visual stimuli. Habituation was performed for one week and mice did not receive any reward under any condition.

In vivo two-photon calcium imaging

Imaging was performed using a two-photon microscope (Bruker Ultima) equipped with resonant galvo scan mirrors controlled by the Prairie software. Images were acquired using a water-immersion 20× objective (N20x-PFH, NA 1, Olympus). A 80-MHz Ti:Sapphire laser (Mai Tai DeepSee, Spectra-Physics) at 950nm was used for excitation of GCaMP6f and td-Tomato. Laser power did not exceed

30 mW under the objective. Fluorescence was detected by a GaAsP PMT (H7422PA-40 SEL, Hamamatsu). Time-series movies of neuronal populations expressing GCaMP6f were obtained at the frame rate of 30.257 Hz (294 × 294 μm, FOV; 0.574 μm/pixel). The duration of each focal plane movie was 330.5 s (10,000 frames). Animals were head-restrained in the dark (with no visual stimuli) and free to locomote on a disk treadmill (30 cm diameter) and kept under the two-photon microscope maximally for 70 min per day. The speed of each mouse on the rotating disk was continuously monitored using a rotary encoder (US Digital; H5-1024-IE-S; 1000 cpr) connected to a digitizer (Axon Digidata 1440, Molecular Devices) and analyzed with custom-written software in Python. Signals were recorded at 2KHz and downsampled to 30 Hz for analysis. For the calculation of speed, we multiplied the perimeter of the disk to the number of turns and then divided by the elapsed time.

To pharmacologically block CB1 we used the inverse agonist SR 141716A (Rimonabant). CB1-tdTomato mice were injected i.p. with Rimonabant (5 mg/kg, TOCRIS) or vehicle (1.25% (vol/vol) DMSO, 1.25% (vol/vol) Tween80 in saline (Bellocchio et al., 2013), 30 min or max up to 1 h, before the onset of the imaging session. After two-photon calcium imaging recordings, we verified post-hoc the area of recording using immunofluorescence. We used the Fiji plug-in BigWarp to superimpose our brain sections with the Paxinos atlas to confirm the area of injection.

Imaging data processing

Motion correction of the two-photon time-series was performed using a registration algorithm built into the Suite2p software. Segmentation into regions of interest (ROIs) was performed with Suite2p, confirmed by visual inspection and fluorescence traces extracted from the green channel for the different ROIs. This algorithm detects mainly active cells (Stringer and Pachitariu, 2019). The number of ROI was similar in the visual areas in all conditions. Ca^{2+} traces were corrected for neuropil contamination. The neuropil mask resembled a band surrounding the ROI with its inner edge having a distance of 3 microns away from the edge of ROI and its outer edge having a distance of 30 microns from the edge of the ROI. The resulting neuropil trace, N, was subtracted from the calcium trace, F, using a correction factor a: Fc(t) = F(t) - a•N(t) where a was defined as 0.7 like previously described (Stringer and Pachitariu, 2019). When we did not correct for neuropil fluorescence, changes of $\Delta F/F_0$ between V1 and V2M were still present. Therefore, neuropil correction did not affect the interpretation of the results (Figure S12). Changes in fluorescence were then quantified as $\Delta F/F_0$. F_0 was calculated using the "Maximin" baselining method from Suite2p where neuropil corrected fluorescence traces are first smoothed using a Gaussian filter (width 60 s) followed by a sliding minimum filtering with a window of 60s, and then maximum filtering with the same time window. Such a running baseline allows to remove slow timescale changes in fluorescence (Stringer and Pachitariu, 2019).

Spike deconvolution and spike tiling coefficient (STTC) calculation

STTC analysis was performed on deconvolved fluorescence traces as previously described (Cutts and Eglen, 2014). Briefly, a nonnegative spike deconvolution was applied to GCaMP6f fluorescence traces using the OASIS algorithm (implemented in Suite2P) with a fixed timescale of calcium indicator decay of 0.7s. Events corresponding to variations in fluorescence with an amplitude lower than 3 times the standard deviation (STDV) of the $\Delta F/F_0$ trace were excluded. The number of events was significantly higher in V2M than V1, both in animal number (Figure S7A, left panel) as well as in individual cells (Figure S7A, right panel). STDV was calculated by fitting a Gaussian process to the negative $\Delta F/F_0$ fluctuations of each ROI (Romano et al., 2017). To quantify the correlation between event trains in pairs of ROIs (A and B), we look for events in A which fall within $\pm\Delta t$ of an event from B. This spike tiling coefficient reduces contribution of different firing rates in estimating correlations in neuronal spike times. The STTC value for sequences of calcium events in two ROIs, A and B, were calculated according to:

$$STTC = \frac{1}{2}\left(\frac{P_A - T_B}{1 - P_A T_B} + \frac{P_B - T_A}{1 - P_B T_A}\right)$$

Where T_A is the proportion of total recording time which lies within $\pm\Delta t$ of any event in A. T_B was calculated in a similar manner. A Δt of 300 ms was used to take into account the slow rise time of GCaMP6f that limits precise temporal estimation of deconvolved events (Stringer and Pachitariu, 2019). P_A corresponds to the proportion of spikes from A which fall within Δt of any spike from B. P_B was calculated similarly. STTC values were calculated for all pairs of ROIs within the same individual field of view. To assess the significance of the correlations we generated for each pair of neurons, 1000 different event sequences (N_{shuff}) where the number of events remained constant (equal to experimental data) but event time was randomly attributed along the total recording period (event shuffling). For each neuron pair (a,b) we calculated a p value of the original $STTC_{a,b}$ (T) as previously reported (Renart et al., 2010):

$$p = \left(N_{pos} + N_{neg}\right)/N_{shuff},$$

where N_{pos} = number of simulated pairs with $STTC > \left|STTC_{a,b}(T)\right|$ and N_{neg} = number of simulated pairs with. $STTC < \left|STTC_{a,b}(T)\right|$

A pair of spike events was deemed statistically significant if $p < 0.05$.

In all our imaging experiments the FOV was 294 × 294 μm (all recordings used a 20× objective with a zoom factor of 2). Given the spread of the axonal plexus of CB1 BCs (Figures 1E and S2H) we assume that one CB1 BC largely covers (and exceeds) the FOV. Knowing that each time series contained ~2–5 td-Tomato-positive cells, we conclude that the activity of a significant fraction of PNs in the FOV is under the influence of >1 CB1 BC.

Spiking network model

We analyzed the effect of CB1 signaling in a numerical model of cortical dynamics: a randomly connected network of artificially-spiking neurons with conductance-based synapses (Vogels and Abbott, 2005; Kumar et al., 2008; El Boustani and Destexhe, 2009; Zerlaut et al., 2019). Single cells were described as single compartment leaky integrate-and-fire models and the synaptic dynamics followed an exponential time course. The dynamics of a single neurons thus followed the set of equations:

$$\begin{cases} C_m \dfrac{dV_m}{dt} = g_L \cdot (E_L - V_m) + \sum\limits_{\{syn\}} g_{syn}(t) \cdot (E_{syn} - V_m) \\ g_{syn}(t) = \sum\limits_{\{t_{syn}, \delta_{syn}\}} \delta_{syn} \cdot Q_{syn} \cdot H(t - t_{syn}) \cdot e^{\frac{-(t - t_{syn})}{\tau_{syn}}} \end{cases} \quad (1)$$

where V_m is the membrane potential of the neuron and C_m its membrane capacitance. The leak currents were set by the leak conductance g_l and leak reversal potential E_L. The synaptic currents (indexed by "*syn*" and summing over its set of source synaptic population for a given neuron type) were set by the time-varying synaptic conductances $g_{syn}(t)$ and the synaptic reversal potential E_{syn}. The synaptic conductances $g_{syn}(t)$ resulted for the convolution of the set of incoming synaptic events $\{t_{syn}\}$ with an exponential waveform of time constant τ_{syn} weighted by the synaptic quantal Q_{syn}. At each synaptic event t_{syn}, we drew a random number δ_{syn} (either 0 or 1) where the release probability at this synaptic connection sets the probability to be 1. The membrane potential dynamics (Equation 1) was complemented with a "threshold and reset" mechanism. When the membrane potential reached the spiking threshold, it was clamped at the reset potential for the duration of the refractory period after which the V_m dynamics restarted from there. Parameters can be found in the table below.

Model design and parametrization steps

Starting from a two population excitatory/inhibitory network, we adapted and parameterized the model in three successive steps to study the impact of the CB1-mediated area-specificity. The two first steps aim at building a V1 model and the last step introduces the CB1-mediated differences with the other cases considered in the study: V2M and V2M with CB1 knockout (V2M-CB1-KO). We started from a sparsely connected excitatory/inhibitory network (parameters as in Zerlaut et al., 2019, see table below) displaying asynchronous dynamics (i.e. regimes of near-zero correlations) in absence of temporally-structured input.

First, we split the inhibitory population into two separate populations to model the PV-positive and CB1-positive population in the L2/3 network (Figures 7A–7C). We modeled the weak/unreliable presynaptic properties of the CB1+ neurons by introducing a release probability variable in synaptic transmission. We kept the cellular parameters (see table), the excitatory couplings ($p_{conn} = 0.05$ for the three populations) and the global inhibitory-to-excitatory coupling constant (i.e. we increased the inhibitory-to-excitatory coupling by 25%, i.e. from $p_{conn} = 0.05$ to $p_{conn} = 0.067$, to compensate for the fact that the CB1 population is 50% less efficient than the initial setting). This left 5 free parameters to set in the model: the two inhibitory-to-inhibitory couplings (the PV-to-PV and CB1-to-CB1 connectivities) and the strength of background activity for the three populations (set as the connectivity parameters between a background Poisson process at a constant 4Hz level and the target population). Those parameters were optimized based on constraints on the levels of activity for the three population model. We performed an exhaustive grid search on this 5 dimensional connectivity space (grid values: $p_{conn} \setminus [0.025, 0.05, 0.075, 0.1]$ for all 5 connectivity parameters) and looked for the configuration minimizing the difference with the following activity configuration: L2/3 PN = 0.5Hz, PV = 20Hz, CB1 = 10Hz (the resulting parameters are shown in the table below).

Second, we introduce a Layer 4 excitatory population (L4 PN) and the L4-to-L2/3 afferent pathway. For simplicity, the L4 PN cellular and synaptic properties were identical as those of L2/3 PN (see table) and we connect L4 PN to L2/3 PN only (Figures 7A–7C) with a connectivity $p_{conn} = 0.01$ (i.e. 40 synapses from L4 per L2/3 neuron). L4 PN receives feedback from CB1 interneurons in L2/3 (see data in Figure 2A) with a low connectivity in the V1 model ($p_{conn} = 0.025$, i.e. smaller than twice the connectivity of CB1-to-L2/3 PN, see data in Figure 2A). L4 PN was weakly stimulated by the constant background drive ($p_{conn} = 0.01$, corresponding to subthreshold stimulation levels, see Figures 7A–7C and 7F) as our experimental setting corresponds to low sensory stimulation (recordings in the dark in the absence of visual stimuli). This last setting was found to be critical to explain the experimentally observed relationship in terms of spontaneous activity and correlations. Indeed, if a too strong fraction of the spontaneous activity in L2/3 is inherited from the spontaneous activity of L4, the effect of CB1 modulation from V1 to V2M can be inhibitory instead of disinhibitory because of the CB1-to-L4 inhibitory feedback (not shown).

Third we introduced the specifics of the different cases in our experimental study. We reduced release probability at the CB1-to-L2/3 PN synapses and increase the CB1-to-L4 PN connectivity to model the V2M case and we increased only the CB1-to-L4 PN connectivity in the V2M-CB1-KO case (see data in Figures 2 and 4). The results of Figure 7 are shown for a reduction and increase factor of 2 (for release probability and connection strength respectively) but spontaneous activity and correlation results were found to be robust to factor variations in the range [1.5–3] (Figure S11).

In addition, we introduce a time-varying input (see Figures 7A–7C) to analyze evoked activity in the circuits. This stimulation has the same synaptic properties as the background stimulation (see table). The time varying rate is obtained by drawing a set of Gaussian waveform events from a Poisson process at 1 Hz with a Gaussian width of 200ms and assigning a random amplitude from a uniform

distribution between 0 and A_{max} = 4Hz. This maximum amplitude level A_{max} was determined as the minimum level where the L2/3 PCs correlations reached the level observed in the V1 data (see Figure 6B, those data were matched to STTC = 0.078 in the V1 model at A_{max} = 4Hz after varying A_{max} from 1 to 7Hz in steps of 0.33Hz, see Figures 7A–7C and 7I).

Numerical simulations and analysis of spiking network dynamics

Numerical simulations were performed with the Brian2 simulator (Stimberg et al., 2019). A time step of dt = 0.1ms was chosen and the numerical integration was done using the "exponential Euler" scheme. The first 200ms of simulation were always discarded from the analysis to remove the contributions of initial transients. Simulations were repeated over N = 20 seeds generating different realizations of the random connectivity scheme and of the time-varying input (Figure 7, see main text). Population rates were evaluated by binning spikes in 5ms bins and were smoothed with a Gaussian of 20ms width (Figures 7A–7C). Correlations were evaluated on spiking activity from 2000 randomly picked L2/3 PN pairs using the Spike Time Tiling Coefficient (STTC) implementation of the Elephant software package (Denker et al., 2018) with a synchronicity window of 300ms. Input-output curves (Figures 7G and S11) were computed by feeding the model (either in L4 PNs or L2/3 PNs, see figure legends) with a set of Gaussian waveforms of increasing amplitude and by taking the average response within the [-50,50]ms interval surrounding the center of the stimulus. The code for the simulating and analyzing the spiking network model is publicly available at https://github.com/yzerlaut/CB1_ntwk_modeling and archived at https://doi.org/10.5281/zenodo.6795090.

Table. Parameters of the spiking network model

Neuronal populations	
Layer 2/3 pyramidal neurons (L2/3 PN)	N = 4000
Layer 2/3 CB1-positive interneurons (CB1)	N = 500
Layer 2/3 PV-positive interneurons (PV)	N = 500
Layer 4 pyramidal neurons (L4 PN)	N = 4000
background/input	N = 4000
Single cell properties (leaky-integrate-and-fire model)	
leak conductance (L2/3 PN, CB1, PV, L4 PN)	10nS
membrane capacitance (L2/3 PN, CB1, PV, L4 PN)	200pF
leak reversal potential (L2/3 PN, CB1, PV, L4 PN)	−70mV
reset potential (L2/3 PN, CB1, PV, L4 PN)	−70mV
spiking threshold (L2/3 PN, L4 PN)	−50mV
spiking threshold (CB1, PV)	−53mV
refractory period (L2/3 PN, CB1, PV, L4 PN)	5ms
Synaptic properties	
excitatory weights (L2/3 PN, L4 PN, background, L4 input)	2nS
inhibitory weights (CB1, PV)	10nS
synaptic decay time (L2/3 PN, L4 PN, background, L4 input, CB1, PV)	5ms
release probability (L2/3 PN, L4 PN, background, L4 input, PV)	1
release probability (CB1 - V1 & V2M-CB1-KO models)	0.5
release probability (CB1 - V2M model)	0.25
Connectivity probabilities	
L2/3 PN to L2/3 PN/CB1/PV	5%
CB1 to L2/3 PN	6.7%
PV to L2/3 PN	6.7%
PV to PV	7.5%
CB1 to CB1	2.5%
background to L2/3 PN	7.5%
background to PV	7.5%
background to CB1	2.5%
L4 PN to L2/3 PN	1%
CB1 to L4 PN (V1 model)	2.5%
CB1 to L4 PN (V2M & V2M-CB1-KO models)	5%
background to L4 PN	1%

QUANTIFICATION AND STATISTICAL ANALYSIS

All statistical analysis were performed in Prism (GraphPad) or OriginPro (2016; OriginLab Co.). The normality of data was systematically tested with a D'Agostino and Pearson omnibus normality test. When normal, two datasets were compared using independent t-tests. When more than two datasets were compared, one-way ANOVAs and two-way ANOVAs were used. In situations where data was not normal or samples were small, we used non-parametric tests (Mann Whitney U test and Kruskal-Wallis test followed by Dunn's multiple comparison test for more than two groups, respectively) unless stated otherwise. For paired comparisons, we used paired t test and Wilcoxon matched-pairs signed rank test for normally and non-normally distributed datasets, respectively. Differences were considered significant if $p < 0.05$ (*$p < 0.05$, **$p < 0.01$, ***$p < 0.001$) and means are always presented with the SEM.